Structural and Electronic Effects of X-ray Irradiation on Prototypical [M(COD)Cl]$_2$ Catalysts

Nathalie K. Fernando,[†] Andrew B. Cairns,[‡] Claire A. Murray,[¶]

Amber L. Thompson,[§] Joshua L. Dickerson,[∥] Elspeth F. Garman,[⊥]

Nayera Ahmed,[†] Laura E. Ratcliff,[‡] and Anna Regoutz[*,†]

[†]*Department of Chemistry, University College London, 20 Gordon Street, London, WC1H 0AJ, UK.*

[‡]*Department of Materials, Imperial College London, Royal School of Mines, Exhibition Road, SW7 2AZ, UK.*

[¶]*Diamond Light Source Ltd, Diamond House, Harwell Science and Innovation Campus, Didcot, Oxfordshire, OX11 0DE, UK.*

[§]*Chemical Crystallography, Chemistry Research Laboratory, University of Oxford, South Parks Road, Oxford OX1 3QR, UK.*

[∥]*MRC Laboratory of Molecular Biology, Francis Crick Avenue, Cambridge Biomedical Campus, Cambridge CB2 0QH, UK.*

[⊥]*Department of Biochemistry, University of Oxford, South Parks Road, Oxford, OX1 3QU, UK.*

E-mail: a.regoutz@ucl.ac.uk

Abstract

X-ray characterisation techniques are invaluable for probing material characteristics and properties, and have been instrumental in discoveries across materials research. However, there is a current lack of understanding of how X-ray induced effects manifest in small molecular crystals. This is of particular concern as new X-ray sources with ever increasing brilliance are developed. In this paper, systematic studies of X-ray-matter interactions are reported on two industrially important catalysts, $[Ir(COD)Cl]_2$ and $[Rh(COD)Cl]_2$, exposed to radiation in X-ray diffraction (XRD) and X-ray photoelectron spectroscopy (XPS) experiments. From these complimentary techniques, changes to structure, chemical environments, and electronic structure are observed as a function of X-ray exposure, allowing comparisons of stability to be made between the two catalysts. Radiation dose is estimated using recent developments to the RADDOSE-3D software for small molecules and applied to powder XRD and XPS experiments. Further insights into the electronic structure of the catalysts and changes occurring as a result of the irradiation are drawn from density functional theory (DFT). The techniques combined here offer much needed insight into the X-ray induced effects in transition metal catalysts and consequently, their intrinsic stabilities. There is enormous potential to extend the application of these methods to other small molecular systems of scientific or industrial relevance.

Introduction

X-ray diffraction and X-ray photoelectron spectroscopy are just two of the many X-ray based characterisation techniques used routinely to probe material properties. The focus of X-ray–matter interaction studies over the past two decades has been macromolecular crystallography, where significant advances have been made in understanding the global and specific radiation damage processes involved during X-ray irradiation of a sample.[1–4] However, the effects of X-ray exposure on the structure and chemistry of small molecular crystals have to date been largely overlooked, despite the early seminal work of Abrahams,

2

and Seiler and Dunitz.[5,6] Furthermore, radiation damage beyond macromolecular systems has not been widely and systematically studied, leading to a serious lack of understanding of radiation-induced changes. This is true not only for small molecular systems but also framework materials, ceramics and alloys, despite experimental experience clearly showing the occurrence of radiation-induced changes in these materials and beyond.[7–9]

In laboratory systems, microfocus methods are increasingly used to generate X-rays from a small spot on the anode target, producing higher intensity X-rays with reduced excess heat generation.[10] One example of new generation laboratory sources is Excillum's liquid metal jet anode. It uses liquid gallium or indium rich alloys, avoiding the typical electron beam damage to the anode in standard solid-metal anode sources. This consequently allows for higher electron beam power with small electron focus resulting in X-rays of very high flux density.[11,12] There has also been growing interest in Inverse Compton Scattering (ICS) laboratory X-ray sources, which produce backscattered X-ray photons from the collision of a relativistic electron beam with a high power laser beam. They aim to achieve small beam sizes with increased tunability and high photon flux density, comparable to that from synchrotron sources.[13,14] In parallel, fourth generation synchrotron light sources are coming into operation: the MAX IV facility in Lund, Sweden (2016);[15] the Sirius synchrotron source in Brazil (2020); and in France, the ESRF's new storage ring, the Extremely Brilliant Source (ESRF-EBS), has recently opened for user operation (2020).[16,17] This new generation of synchrotrons incorporates technologies such as multibend-achromat (MBA) lattices and compact magnet designs to achieve ultra low-emittance and therefore higher brightness X-ray beams.[15,16] For instance, a double triple bend achromat (DTBA) magnetic lattice is planned to be installed as part of Diamond Light Source's Diamond-II upgrade, enabling higher photon flux densities to be achieved.[18,19] In addition, the new lattices deliver X-rays with higher coherence, enabling the move from micro- to nanofocus beams, which further exacerbates radiation damage challenges. One example is the recently installed X-ray diffraction endstation on beamline ID11 at the ESRF-EBS, capable of reaching photon energies

3

in the 30–70 keV range with a nano-focus beam size of 150–500 nm. With a beam size of less than 200 nm, a flux of approximately 1.75×10^{11} photons/second can be achieved.[20] A growing number of next generation X-ray Free Electron Lasers (XFELs) are also coming into operation, capable of producing ultra short (fs), coherent pulses of X-ray radiation of superior brilliance, such as the European XFEL in Germany, which opened for users in 2017.[21]

Given the vast developments in X-ray source technologies, understanding the radiation damage processes and possible mitigation methods is more important than ever. Major developments in the understanding of radiation damage in macromolecular crystallography (MX) have enabled the emergence of mitigation strategies, such as sample cryocooling, beam attenuation, and the incorporation of molecular radioprotectants and scavengers, among others.[22–26] In addition, the development of RADDOSE-3D, an X-ray dose estimation tool, by Garman and coworkers has enabled quantitative estimations of X-ray doses causing the observed perturbations in structure.[27,28] Dose is defined as the energy absorbed per unit mass of sample (J/kg=Gy, gray). In recent years, several additions have been implemented into the RADDOSE-3D utility to extend its application beyond the standard MX experiment. For instance, Brooks-Bartlett *et al.*[29] incorporated tools to apply the software to biological Small Angle X-ray Scattering (SAXS) experiments, Christensen *et al.*[7] added options for modelling X-ray dose in small molecules and Dickerson *et al.* integrated time stamping of the ionisation events for tracking XFEL pulse effects.[30]

In addition, there are a few early reports of sample damage in small molecular crystals, specifically in iridium complexes, e.g. an XPS study by Mason *et al.* in 1972 of d^8 and d^{10} metal complexes revealed the difficulty in obtaining reliable binding energy data for such systems.[31] The Ir^{+1} complexes studied were found to undergo radiation damage, with the Ir^{+1} chlorocomplexes particularly susceptible to severe radiation damage.

The small molecular crystals of interest in the present study are two members of the family of $[M(COD)Cl]_2$ prototypical catalysts, where M= Ir^{+1} or Rh^{+1} and COD= 1,5-

cyclooctadiene. These dimers have important industrial applications as catalysts and catalyst precursors, and as such, make good model compounds. $[Ir(COD)Cl]_2$ is routinely used as a catalyst in carbon-carbon and carbon-heteroatom bond formations, in addition to alkylation, hydrogenation and hydroamination reactions.[32,33] It is also commonly used as a precursor to Crabtree's catalysts.[34] $[Rh(COD)Cl]_2$ is used for carbon-carbon/heteroatom formation and has further applications as a precursor in hydrogenation and cross-coupling reactions.[35]

Both the Ir and Rh systems are binuclear metal d^8 coordination complexes with square planar geometry, sharing an edge in the Cl – Cl plane (see Figure 1(c)). The Ir complex is polymorphic with either an orthorhombic $Pbca$ space group (red-ruby colouration) or a monoclinic Cc or $C2/c$ space group (yellow-orange colouration).[36–38] The Ir sample used for the experiments reported here had the orthorhombic $Pbca$ form as determined from a single crystal X-ray diffraction (SCXRD) analysis, the results of which are presented in Table S1 and Figure 1(a) shows a schematic of the unit cell. The Rh complex crystallised in the monoclinic $P2_1/n$ space group, and its structure was also determined from SCXRD structure solution with the unit cell presented in Figure 1(b). The unit cell of the Ir catalyst contains eight individual molecular units, corresponding to a total of 352 atoms, whereas the Rh unit cell contains four molecular units, corresponding to 176 atoms. The Ir catalyst also has a distinctly folded central Ir – Cl rhombus about the bridging Cl atoms, in comparison with the relatively planar Rh – Cl rhombus of the Rh catalyst. There are similarities however in the atomic or site densities. Both catalysts have a site density of approximately 0.10 sites/Å^3, with comparable packing efficiencies. These samples, both with the same ligand structure, were chosen as a base group to better understand the difference in radiation effects between catalysts with two different metal centres and comparable valence electronic structure.

Despite their electronic similarities, the Ir and Rh catalysts have varying absorption coefficients at the photon energies used in the X-ray characterisation methods presented in this study. This gives rise to substantial differences in the absorbed X-ray dose over the same

period of time between the two systems despite being exposed to the same beam flux. At 18 keV, the routine wavelength at beamline I19, Diamond Light Source, the mass absorption coefficients of the Ir and Rh catalysts are 56.1 cm^2/g and 10.7 cm^2/g, respectively, whereas at 1.487 keV, the corresponding mass absorption coefficients are 1416 cm^2/g for the Ir catalyst and 1457 cm^2/g for the Rh catalyst.[39]
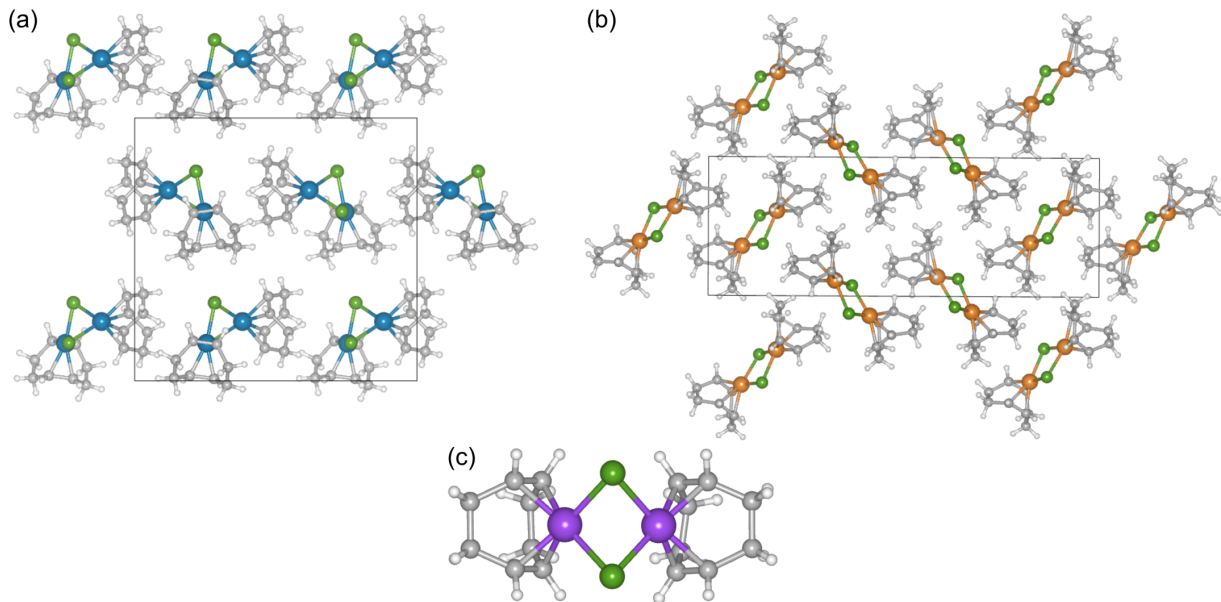

Figure 1: The crystal structures of (a) orthorhombic [Ir(COD)Cl]$_2$ viewed along the b axis, and (b) monoclinic $P2_1/n$ [Rh(COD)Cl]$_2$ viewed along the a axis. The blue, orange, green, dark grey, and light grey atoms correspond to Ir, Rh, Cl, C and H, respectively. The boundaries of the unit cells are also presented. (c) The molecular structure of both catalysts. The purple atoms represent either the Ir or Rh atoms.

Studying the impact of X-ray irradiation on the structure and chemical environments of these catalysts, which have wide reaching applications in the chemical industry, will give much needed insight into their overall stability and behaviour. To gain a better under-standing of the irradiation induced processes, this study employs a combination of X-ray diffraction, X-ray photoelectron spectroscopy, and density functional theory for a systematic exploration of the crystal structure, chemical environments, and electronic structure as a function of sample irradiation. RADDOSE-3D is applied to powder XRD and, for the first time, to XPS experiments to determine the dose absorbed by the samples at the synchrotron

XRD beamline and in the laboratory XPS system.

Experimental Methods

Samples of 1,5-cyclooctadiene-iridium(I) chloride and 1,5-cyclooctadiene-rhodium(I) chloride were acquired as powders from Sigma Aldrich (reference IDs: 683094 and 227951) with purity levels of 97% and 98%, respectively.

Powder X-ray diffraction (PXRD) measurements were conducted on the high resolution PXRD beamline I11 at Diamond Light Source, Didcot, UK.[40] Samples as supplied were ground and placed in 0.3 mm diameter borosilicate capillaries, and measured at a photon energy of 18 keV, equivalent to a wavelength of 0.689 Åand at a temperature of 300 K in transmission geometry. The Mythen II position sensitive detectors (PSD) were used to collect 500 diffraction patterns at regular intervals over a total of two hours of continuous X-ray exposure.[41] Crystal structure analysis was carried out using a combination of batch Le Bail and Rietveld refinements, within the TOPAS version 7 software package.[42,43] Additional parameters within each refinement, such as the zero error value and the isotropic thermal parameters for each atom present, were allowed to refine. Hydrogen atoms were omitted to avoid further complicating the structures and introducing errors into the refinements. M – Cl and C – C distance restraints were applied to achieve a reasonable starting structure and were maintained for the rest of the refinements. $[Ir(COD)Cl]_2$ and $[Rh(COD)Cl]_2$ were also characterised using SCXRD experiments at beamline I19 at Diamond Light Source, Didcot, UK, at an energy of 18 keV (0.689 Å), temperature of 300 K, and a beam transmission of 0.05%.[44] 18 keV was chosen as this is the standard photon energy of beamline I19, and offers a good compromise for accessing absorption edges across all elements. A total of 1500 images were collected in a single 300° phi scan for each catalyst to maintain a consistent illuminated volume for the dose-dependent study. Data were integrated using the *CrysAlis Pro* program and subsequent structure solution and refinement in the *Olex2* software.[45,46]

Further details can be found in the Supplementary Information.

X-ray photoelectron spectra were collected on a Thermo Scientific K-Alpha+ spectrometer at Imperial College London, London, UK. The spectrometer outputs a microfocused Al Kα beam at 1486.7 eV photon energy, operating at 12 kV electron beam potential and 6 mA emission current. An X-ray spot size of 400 μm was used for this experiment. The photon flux at these experimental parameters is calculated to be approximately 3.8×10^{10} photons/s from source parameters obtained from the manufacturers. The catalyst powders were mounted using conductive carbon tape and the spectrometer flood gun was used to compensate for any sample charging. The base pressure of the spectrometer was 2×10^{-9} mbar. The progression of X-ray induced effects was followed by collecting spectra at regular intervals over a total exposure time of 35 h. The acquired photoelectron spectra were the survey, valence band and core level spectra, comprising of Cl 2p, C 1s and the main metal core levels, Ir 4f and Rh 3d, for [Ir(COD)Cl]$_2$ and [Rh(COD)Cl]$_2$, respectively. The survey spectra were obtained at 200 eV pass energy, whilst subsequent core level spectra were collected at a pass energy of 20 eV and a dwell time of 50 ms. The higher resolution valence band spectra were collected at a pass energy of 15 eV and a dwell time of 75 ms. After the first group of spectra were collected, with an acquisition time of approximately one hour, the X-ray beam was left to irradiate the samples for a further hour. This procedure was repeated 18 times, giving a total experiment time of 35 h. The 1 h final wait time was omitted. The *Multiplex* function on the Thermo Scientific data acquisition and analysis software *Avantage* was used throughout the experiment, ensuring an equal distribution of X-ray dose within each measurement group. The *Multiplex* function allows measurement loops of single spectra of each spectrum type until the required total number of scans have been collected.

The *Avantage* software was subsequently used for the peak fitting analysis and quantification of the acquired spectra. The *Smart* background, a development of the Shirley background, was used in combination with a Voigt line shape.[47] The full width half maximum (FWHM) and Lorentzian/Gaussian ratios of the Voigt peaks were refined. Peak fits

were carried out for all 18 iterations to quantify the relative atomic percentages and to determine how the chemical composition, line shapes, and various oxidation states change as a function of irradiation time and dose. The spin-orbit splitting constraints on the peak positions were based on the average published values from the NIST X-ray Photoelectron Spectroscopy database.[48] For the Ir $4f$ doublet a spin-orbit splitting of 3.0 eV was used,[49,50] and for the Rh $3d$ doublet a spin-orbit splitting of 4.7 eV was used.[51] A separation of 1.6 eV was applied to the Cl $2p$ doublet.[52] The doublet peak ratios for both the metal and the Cl $2p$ core level spectra were constrained according to the atomic sensitivity factors. The first set of core-level spectra of [Rh(COD)Cl]$_2$ comprising Rh $3d$, Cl $2p$ and C $1s$ show a consistent systematic shift of approximately 0.3 eV towards lower binding energies relative to the $t = 2$ h spectra (see Figure S14 in the Supplementary Information for the raw data). This is most likely due to initial changes to the powder surface upon introduction into UHV and onset of irradiation, such as the desorption of gas molecules from the surface. To aid comparison, all $t = 0$ h [Rh(COD)Cl]$_2$ spectra are therefore shifted by +0.3 eV.

So that the effects of X-ray irradiation during XRD and XPS experiments could be compared, values for the absorbed X-ray dose are determined using the RADDOSE-3D utility, conventionally used for macromolecular crystallography (MX) beamlines, developed by Garman et $al.$[27,28] It estimates X-ray dose based on the beam and crystal characteristics and was recently adapted for small molecule crystallography, and this option is used here.[7] Dose absorbed during powder X-ray diffraction experiments was estimated using the Diffraction Weighted Dose (DWD) metric.[53] Contrary to typical MX experiments, where the X-ray beam directly irradiates the crystal, powder diffraction experiments require the samples to be mounted in capillaries. A development to RADDOSE-3D by Brooks-Bartlett et $al.$ for capillary samples is therefore employed.[29] For the dose estimates, the calculation of possible fluorescent escape from the crystal is also included in RADDOSE-3D, since this emission of energy from the sample reduces the absorbed dose. The probability of Auger electron emission decreases and the shell fluorescent yield increases as the electron binding energy

increases, and thus fluorescent escape is important for the Iridium L shell. This feature was previously included in RADDOSE[54,55] and has recently been incorporated into RADDOSE-3D. The assumption in RADDOSE that the fluorescent photons were produced in the centre of the crystal has now been removed in RADDOSE-3D, with fluorescence being released along several tracks in all directions from every voxel. For each element, the average wavelength of K shell fluorescence (calculated by weighting the relative proportions of Kα and Kβ fluorescence) is obtained along with the average wavelength of fluorescence from all the L shells.[56] The cross sections can thus be calculated, and based on the distance to the edge of the crystal for each track in every voxel, the probability of escape is then computed for each rotation angle.

This study also presents the first application of RADDOSE-3D to XPS experiments. Dose is estimated using the Average Dose Whole Crystal (AD-WC) metric, which is defined as the total energy absorbed divided by the mass of the whole crystal. This metric is chosen since the same flat sample area is irradiated for the duration of the experiment, and the FWHM of the X-ray beam is such that the entirety of individual crystals is irradiated by the beam. A tabulated summary of the main input parameters for [Ir(COD)Cl]$_2$ and [Rh(COD)Cl]$_2$ used in all RADDOSE-3D calculations and further detailed discussions on dose calculations are given in Table S2 and the related text in the Supplementary Information.

Computational Methods

Solid state density functional theory (DFT)[57,58] calculations were performed with the CASTEP[59] plane-wave pseudopotential code, using the semi-local PBE exchange-correlation functional[60] and on-the-fly generated norm-conserving pseudopotentials, with 17 (15) valence electrons for Rh (Ir). Calculations were performed using a cut-off energy of 900 eV, which was chosen such that the total energy was converged to within 5 meV/atom, and a Monkhorst-Pack k-point grid of $2 \times 1 \times 2$ for [Rh(COD)Cl]$_2$,[61] while [Ir(COD)Cl]$_2$ calculations were performed

at the Γ-point only. Both the atomic positions and unit cell were relaxed, using the semi-empirical dispersion correction scheme of Tkatchenko-Scheffler and applying a maximum force tolerance of 0.02 eV/Å.[62]

Following the geometry optimisations, a single molecule was extracted from each crystal on which calculations were performed without any further relaxation. Gas phase molecule calculations were then performed in free boundary conditions using the wavelet-based BigDFT code,[63] with a grid spacing of 0.212 Å and coarse and fine grid multipliers of 5 and 8, respectively. Calculations employed both PBE and the hybrid PBE0 functional.[64] HGH-GTH pseudopotentials were used,[65,66] with 17 valence electrons for both Rh and Ir.

The projected densities of states (PDOS) for both CASTEP and BigDFT were generated using a Mulliken-style population analysis.[67] The CASTEP PDOS were post-processed using OptaDOS.[68] Gaussian smearing of 0.44 eV was applied to both BigDFT and CASTEP calculations to reflect the experimental resolution. Scofield photoionisation cross-section corrections for an energy of 1.48667 keV were applied using Galore.[69–71] To further aid comparison between theory and experiment, the calculated weighted PDOS intensities were normalised with respect to the maximum intensity of the experimental VB, with a Shirley background subtracted. For the Rh catalyst, the main VB feature is found at a BE of 2.3 eV. In the case of the Ir catalyst, where the PDOS shows two high intensity features, the average height of the two features was used. To align the energy scales of both theory and experiment, a linear fit of the leading VB edge was applied to the experiment. The PDOS were then shifted to align with the half maximum position from the linear fit. The applied shifts to theory were +1.34 eV and +1.92 eV for the Ir and Rh catalysts, respectively.

Results & Discussion

To date, four published structures of $[Ir(COD)Cl]_2$ are available on the Cambridge Structural Database, two of which are of the monoclinic form,[37,72] and the remaining two are

orthorhombic (*Pbca*, 61).[36,38] In order to verify the lattice parameters and to provide a starting point for PXRD analyses, structure solutions for both catalysts from SCXRD data were independently carried out. The measured lattice parameters and ORTEP diagrams for both catalysts are presented in Table S1 and Figures S1 and S2 of the Supplementary Information. The lattice parameters determined for $[Ir(COD)Cl]_2$ from SCXRD match those of the published CIFs mentioned above. It should be noted that different cell settings were used in these structures such that the lattice parameters appear interchanged.[38] The lattice parameters determined from SCXRD refinement of $[Rh(COD)Cl]_2$ agree well with two most recently published structure files on the CSD from Hill *et al.* and Zavalij *et al.*.[73,74] Lattice parameters of both catalysts were extracted with confidence that both structures were undamaged, based on the radiation dose estimations for beamline I19. Beam parameters reported in Christensen *et al.* were used,[7] and the total radiation dose was found to be insignificant in comparison to values for synchrotron PXRD and laboratory XPS. The comparative dose plots for beamlines I11 and I19 are presented in Figure S3 of the Supplementary Information. The fundamental optics and wide ranging experimental capabilities of beamlines lead to considerable variation in radiation dose absorbed by samples irradiated at different X-ray facilities. Special care must therefore be taken when drawing conclusions from multimodal experiments. In this experiment, the significantly lower photon flux (five orders of magnitude) of I19 compared to I11, combined with the shorter total acquisition time (5 min for I19 compared to the unconventional 2 h measurement period at I11), correspond to an X-ray dose (0.9 MGy and 0.3 MGy for the Ir and Rh catalysts, respectively), that is too low to cause any significant global impact on the structure of either $[Ir(COD)Cl]_2$ or $[Rh(COD)Cl]_2$ (see Figure S3).

The lattice parameters obtained from SCXRD were used as a starting point for profile and structural refinements of the first data sets of the 500 powder XRD patterns collected. The first few high intensity, low angle diffraction peaks for $[Ir(COD)Cl]_2$, plotted in Figures 2(a) and (c) as continuous and discrete data, show a heavy loss in peak intensity, a shift in peak

positions, and peak broadening with increasing dose. It is interesting to note that not all reflections behave in the same manner with e.g. the (002) reflection being rather stable, whilst the (020) reflection changes dramatically with dose. In contrast, the comparable data set for $[Rh(COD)Cl]_2$, see Figures 2(b) and (d), shows more subtle changes with radiation dose. To investigate these initial observations in more detail and to enable quantification of the observed changes, batch Le Bail refinements were performed on the 500 powder diffraction patterns for both $[Ir(COD)Cl]_2$ and $[Rh(COD)Cl]_2$. Figure 3 shows the changes in peak area, FWHM, and peak position across the two hour measurement period with increasing cumulative dose. The substantial change in the $[Ir(COD)Cl]_2$ peak area noted in the initial observation can now be quantified as a 16-38% drop in peak area after a dose of 2903 MGy (see Figure 3(a)). The small discontinuities observed in the data can be attributed to changes in beam current associated with the top-up mode of the synchrotron storage ring. Figure S8 in the Supplementary Information shows the correlation between these decreases and the beam intensity. The peak area plot for $[Rh(COD)Cl]_2$ (see Figure 3(d)) confirms that no significant changes are observed over time (dose of 1011 MGy).

Changes to the FWHM of the line shape also vary drastically between the two catalysts with increasing X-ray dose, see Figures 3(b) and (e) for $[Ir(COD)Cl]_2$ and $[Rh(COD)Cl]_2$, respectively. Whilst the Bragg peaks of $[Rh(COD)Cl]_2$ show no significant change in FWHM across the dose range of the measurement time, the change in FWHM of $[Ir(COD)Cl]_2$ is clear, given the greater absorbed dose, and varies considerably across the different reflections. Changes to the FWHM of the Rh catalyst are found to be sensitive to the top up of the storage ring, evidenced by noticeable periodic discontinuities in Figure 3(e). The FWHM of the (210) reflection increases by approximately 40% in contrast to the minimal 4% change in the FWHM of the (002) reflection, at a maximum dose of 2903 MGy. The general broadening of peaks, as well as preferential broadening along certain planes, could be indicative of an increase in disorder within the system. Preferential broadening of the type observed here can also be the result of peak splitting due to symmetry lowering, resulting in asymmetric
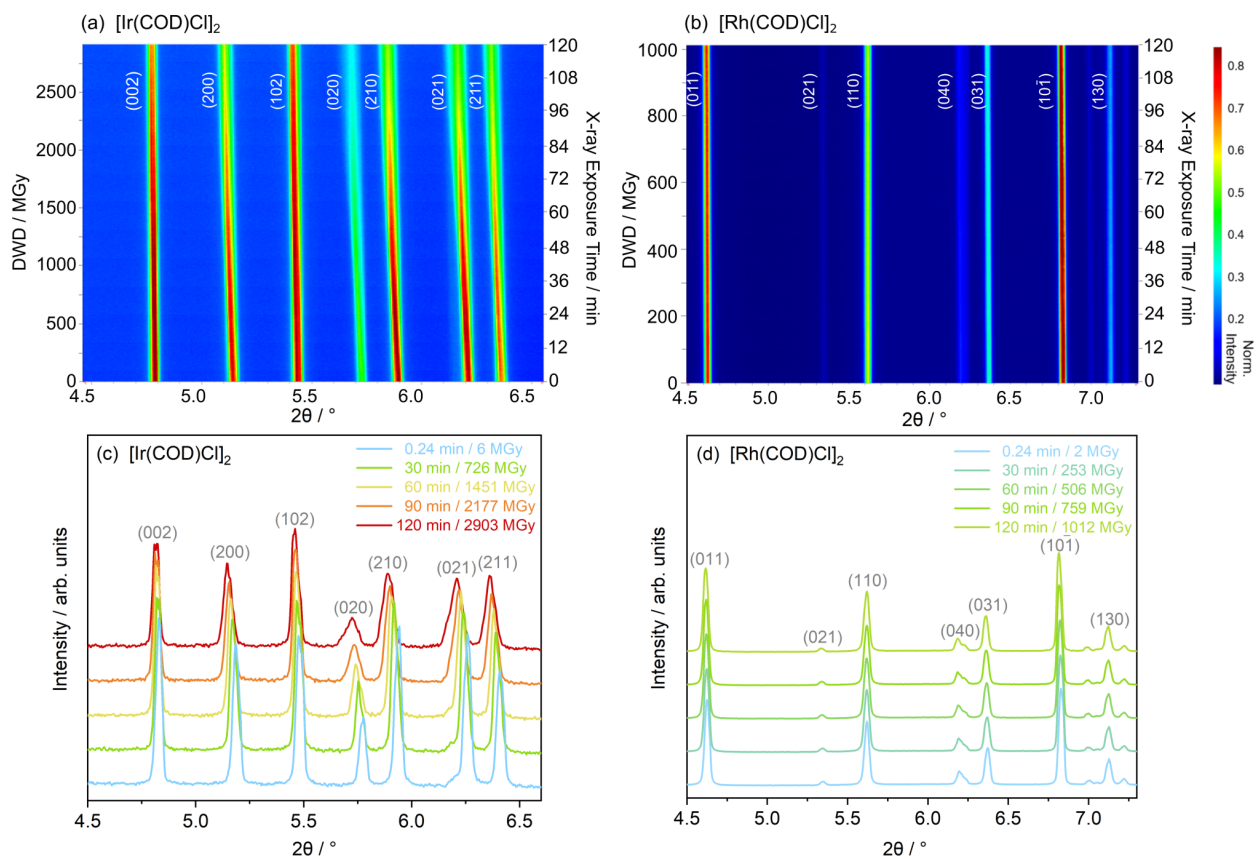
13

Figure 2: Low-angle region of the PXRD patterns collected for both catalysts, as a function of X-ray exposure time and diffraction weighted dose (DWD). (a) and (b) 2D continuous maps of all 500 diffraction patterns for Ir(COD)Cl]$_2$ and [Rh(COD)Cl]$_2$, respectively. (c) and (d) Discrete patterns in 30 min intervals for (c) Ir(COD)Cl]$_2$ and (d)Rh(COD)Cl]$_2$, respectively.

profiles. To further explore this possibility of a radiation-induced phase transition, data were refined using ISODISTORT.[75,76] The parent unit cell model (at minimum dose) was used to find the relevant subgroup. The lower symmetry monoclinic $P2_1/n$ subgroup of $Pbca$, given by the Γ_2^+-point irrep strain mode,[75] and the corresponding symmetry distortion parameters, was found to give a satisfactory fit to the maximum dose diffraction pattern. The subgroup and supergroup lattice parameters have the following relationship: $a' = b$, $b' = c$ and $c' = a$, with the β angle being allowed to refine. The broadening observed in peak (020) in particular, after 2903 MGy of radiation, could only be accounted for when all possible carbon distortion modes, associated with the COD ligand were refined, by conducting symmetry mode Rietveld refinement in $P2_1/n$ of the final data set. Due to the almost negligible change in the monoclinic β angle when refined, it can be assumed that at the end of the two hour irradiation period (2903 MGy), the system had only undergone a very subtle phase transition or this transition was driven by disorder in specific crystallographic directions. The batch refinements were repeated, instead being constrained to the original space group ($Pbca$) and the Ir – Cl and C – C interatomic distances were allowed to refine within the defined restraints. Since the monoclinic refinement conducted could not account for other, more subtle peak splitting, for instance, observed in peak (002), confidence in the final structure could not be justified. In addition, the overall trends in the bond lengths and angle changes were comparable across both spacegroups. Therefore, the high symmetry, fixed orthorhombic set of refinements was used in the following analyses.

The peak positions of the selected high intensity Bragg peaks for both $[\mathrm{Ir(COD)Cl}]_2$ and $[\mathrm{Rh(COD)Cl}]_2$ decrease continuously towards lower 2θ angles from the onset of irradiation (see Figure 3(c) and (f)). The rate of peak shift varies considerably across the two catalysts and across the five reflections presented. The maximum peak shift at a dose of approximately 1012 MGy is observed for the (020) reflection of $[\mathrm{Ir(COD)Cl}]_2$, where a total relative shift of -0.35%, from 5.777° to 5.757°, is observed. This is markedly higher than the maximum shift of -0.16%, from 6.827° to 6.816°, seen at the same dose, for reflection $10\bar{1}$ of $[\mathrm{Rh(COD)Cl}]_2$.
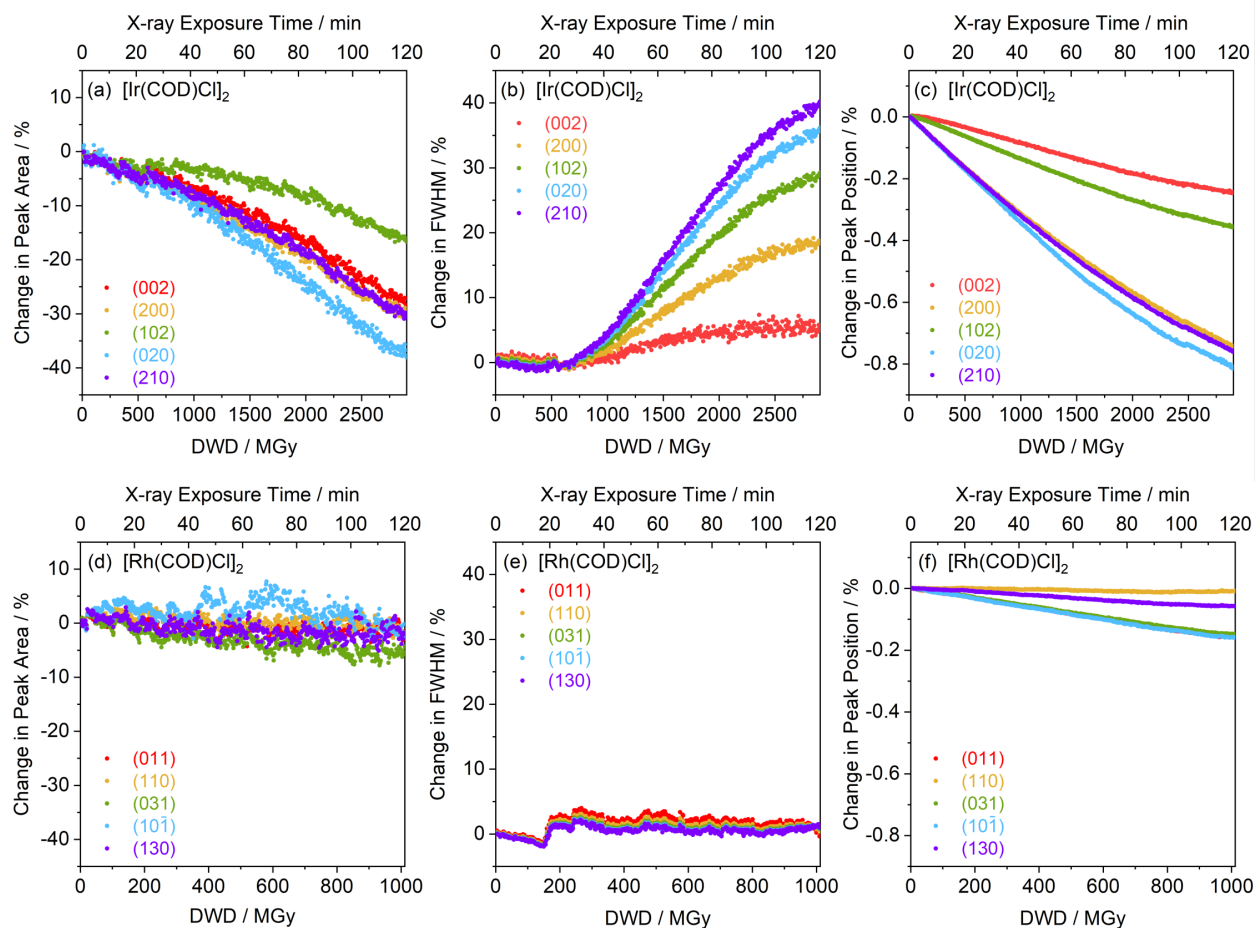
Figure 3: Quantitative results extracted from Le Bail refinements of the PXRD data, including the relative changes in (a) and (d) peak area, (b) and (e) FWHM, and (c) and (f) peak position. The top row of graphs (a)-(c) show the results for $[Ir(COD)Cl]_2$ and the bottom row of graphs (d)-(f) the results for $[Rh(COD)Cl_2]$, respectively. All plots include both the X-ray exposure time as well as the calculated X-ray dose as Diffraction Weighted Dose (DWD) from RADDOSE-3D.

Peak shifts towards smaller angles are a result of a unit cell expansion, and the percentage change in lattice parameters, obtained from the Le Bail refinements, as a function of dose and irradiated time for $[Ir(COD)Cl]_2$ and $[Rh(COD)Cl]_2$ is presented in Figure 4. For $[Ir(COD)Cl]_2$, the a and b lattice parameters undergo an increase of approximately 0.8% of the original values, compared to the mere 0.2% increase in c. In contrast, $[Rh(COD)Cl]_2$ shows little change with prolonged irradiation, with the b and c lattice parameters increasing by under 0.2%, whilst the a parameter increases by just 0.004%. The β lattice parameter sees a 0.12% increase over the same dose of 1012 MGy, see Figure S11 of the Supplementary Information.

Comparing the change in overall unit cell volumes of the two catalysts in Figure 4(c), a 1.9% increase in $[Ir(COD)Cl]_2$ and 0.3% increase in $[Rh(COD)Cl]_2$ unit cell volumes after a total dose of 2903 MGy and 1012 MGy, respectively, is observed. Although the measurement conditions were identical for both catalysts, the estimated dose differs significantly with an increase of 24 MGy/min for $[Ir(COD)Cl]_2$, and of 8 MGy/min for $[Rh(COD)Cl]_2$, meaning that the Ir catalyst absorbs 100 MGy of X-ray dose after only 4 min of measurement time, whilst it takes more than three times as long for the Rh catalyst to receive the same dose (after 12 min) because of the large difference in absorption coefficients at this incident X-ray energy. Comparing the unit cell changes as a function of dose provides a more robust method of comparing the stabilities of the Ir and Rh catalysts. For instance, at a dose of 1012 MGy (equivalent to 36.5 min), the Ir catalyst undergoes an overall unit cell volume increase of 0.7%, compared to the 0.3% increase in the Rh sample at the same dose compared to the volumes measured at the lowest dose. The changes in lattice parameters at the same dose of 1012 MGy, show a similar trend, with the Ir lattice parameters expanding at a faster rate, with the exception of the c parameter, which sees a very small (0.07%) increase. From these observations, it is clear that overall the $[Ir(COD)Cl]_2$ unit cell shows significant instability during PXRD experiments, in contrast to the relatively robust behaviour of $[Rh(COD)Cl]_2$.

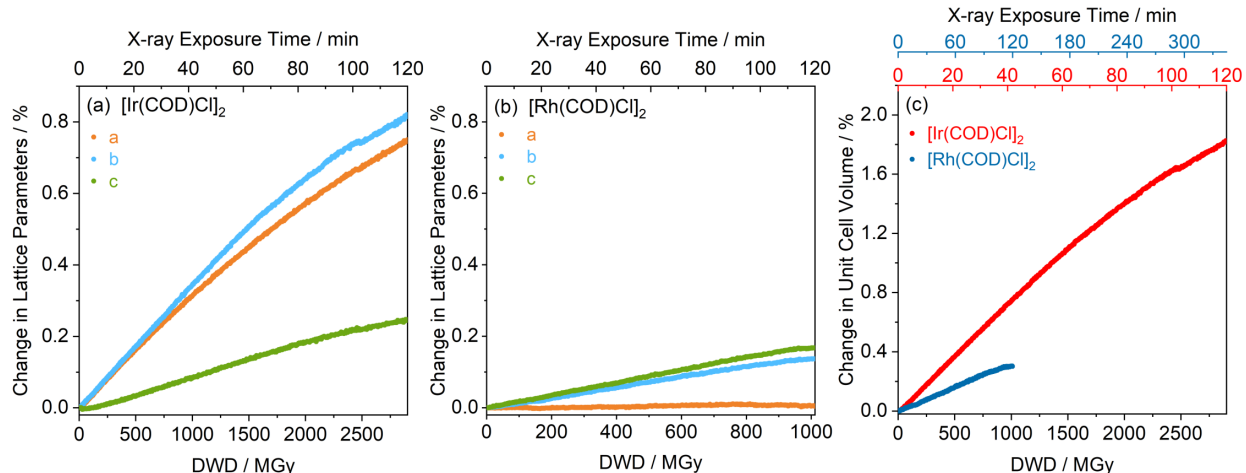In order to better understand the global changes to atomic positions, and consequently,

Figure 4: Relative changes to the unit cells of $[Ir(COD)Cl]_2$ and $[Rh(COD)Cl]_2$. (a) and (b) show the changes to the lattice parameters a, b and c for (a) $[Ir(COD)Cl]_2$ and (b) $[Rh(COD)Cl]_2$, respectively. (c) shows the changes to the unit cell volume of both catalysts. All plots include both the X-ray exposure time as well as the calculated X-ray dose as Diffraction Weighted Dose (DWD) from RADDOSE-3D.

bond lengths and angles, caused by the irradiation, batch Rietveld refinements of both $[M(COD)Cl]_2$ catalysts were performed. The refinements of the first and last diffraction patterns are included in Figures S4-S7 in the Supplementary Information. As expected based on the data analysis so far, changes to both bond lengths and angles are more pronounced in $[Ir(COD)Cl]_2$ compared to $[Rh(COD)Cl]_2$. The extracted first (after 14 s of X-ray exposure) and last (after 2 h of irradiation) selected bond angles and lengths, along with the relative differences and relevant doses, are summarised in Tables 1 and 2, respectively.

A marked increase in the Cl – M – Cl bond angles of the Ir catalyst is observed, where the Cl1 – Ir1 – Cl2 and Cl1 – Ir2 – Cl2 angles expand by 6.4% and 8.3%, respectively. The Rh catalyst shows much smaller angular changes of at most 0.3%. Meanwhile, a subtle decrease of -0.5% and -1.5%, in the M – Cl – M bond angles occurs in the Ir catalyst. Whilst the Rh catalyst shows almost no overall change in bond length, the Ir catalyst undergoes a prominent global extension in the Cl1 – Cl2 distance of 5.2%, accompanied by a 2.0% decrease in the M1 – M2 distance. The overall combination of these observed effects results in the flattening of the central Ir – Cl motif about the M – M axes in $[Ir(COD)Cl]_2$. Whilst clear

18

Table 1: The bond angles ϕ and relative changes obtained from Rietveld refinements of the first and last PXRD patterns at the start (14 s, equivalent to 6 MGy for the Ir and 2 MGy Rh catalyst) and at the end (2 h, equivalent to 2903 MGy and 1012 MGy, respectively) of irradiation time. The atomic labels used are defined in Figures S1 and S2 in the Supplementary Information.

Catalyst	Atoms	ϕ_{start} / °	ϕ_{end} / °	change / %
	Cl1 − Ir1 − Cl2	80.8(5)	86(1)	+6.4
	Cl1 − Ir2 − Cl2	80.3(5)	87(1)	+8.3
[Ir(COD)Cl]$_2$	Ir1 − Cl1 − Ir2	74.8(4)	74.4(9)	−0.5
	Ir1 − Cl2 − Ir2	75.1(4)	74(2)	−1.5
	Cl1 − Rh1 − Cl2	83.7(3)	83.5(3)	−0.2
	Cl1 − Rh2 − Cl2	82.9(3)	82.8(3)	−0.1
[Rh(COD)Cl]$_2$	Rh1 − Cl1 − Rh2	95.4(3)	95.5(3)	+0.1
	Rh1 − Cl2 − Rh2	96.8(1)	97.1(3)	+0.3

Table 2: The interatomic distances d and relative changes obtained from Rietveld refinements of the first and last PXRD patterns at the start (14 s) and at the end (2 h) of irradiation time. The atomic labels used are defined in Figures S1 and S2 in the Supplementary Information.

Catalyst	Atoms	d_{start} / Å	d_{end} /Å	change / %
	Ir1 − Ir2	2.907(4)	2.85(1)	−2.0
	Cl1 − Cl2	3.09(2)	3.25(5)	+5.2
[Ir(COD)Cl]$_2$	Ir1 − Cl1	2.41(1)	2.41(3)	0.0
	Ir1 − Cl2	2.35(1)	2.33(5)	−0.9
	Ir2 − Cl1	2.37(2)	2.30(3)	−2.9
	Ir2 − Cl2	2.42(2)	2.41(6)	−0.4
	Rh1 − Rh2	3.489(4)	3.483(4)	−0.2
	Cl1 − Cl2	3.12(1)	3.1(1)	−0.6
[Rh(COD)Cl]$_2$	Rh1 − Cl1	2.355(8)	2.353(9)	−0.1
	Rh1 − Cl2	2.316(8)	2.309(7)	−0.3
	Rh2 − Cl1	2.363(8)	2.354(8)	−0.4
	Rh2 − Cl2	2.348(7)	2.339(7)	−0.4

trends are seen for $[Ir(COD)Cl]_2$, the changes are too subtle to draw definitive conclusions for $[Rh(COD)Cl]_2$. These results from Rietveld refinements further underline previous observations on the instability of $[Ir(COD)Cl]_2$ under the same experimental conditions compared to the relative robustness of the Rh catalyst, after absorption of the same X-ray dose. It should be noted that the absolute values of the Cl — Cl bond length increase and Ir — Ir decrease, with increasing dose, is dependent on the level of restraints applied to the positions of the carbon atoms comprising the COD structures. This is evidenced by test refinements conducted, from fully fixed to refined COD positions with appropriate distance restraints, throughout the 500 consecutive data sets. The overall trend of the movements of the central Ir — Cl rhombus and simultaneous flattening, however, is consistent in all cases.

XRD provides an average picture of the change in crystal structure and the average changes to bond lengths and angles. However, to understand local changes in both chemical environment and electronic structure in more detail, core and valence level XPS was used. The direct comparison of the two X-ray techniques, including radiation effects and damage progression with dose, is able to provide a more complete picture of the changes and differences observed for $[Ir(COD)Cl]_2$ and $[Rh(COD)Cl]_2$. To enable this comparison, X-ray dose is an invaluable metric by which to understand the extent of radiation-induced effects across both characterisation methods. The calculated doses for PXRD and XPS for both the Ir and Rh catalysts as a function of irradiated time is presented in Figure 5. Figure 5(a) shows that the $[Ir(COD)Cl]_2$ diffraction weighted dose (DWD) in PXRD experiments is approximately four times that for $[Rh(COD)Cl]_2$ at a given exposure time. This significant discrepancy between the two seemingly similar catalysts is due to the their respective absorption coefficients at the photon energy used in the diffraction experiments. The incident X-ray energy of 18 keV intersects the tail of the Ir L absorption edges (11.2-13.2 keV),[77] whilst no Rh absorption edges are in the vicinity of this energy. Therefore, the absorption coefficient of the Ir catalyst is higher than at lower incident X-ray energy, and so absorbs an even greater amount of photon energy per unit mass. The total average dose (whole crystal)

(AD-WC) calculated for the XPS experiment is one to two orders of magnitude less than the total DWD calculated for XRD. This is predominantly due to the three orders of magnitude greater photon flux at the synchrotron versus the laboratory spectrometer. In addition, the excitation energies differ significantly between the PXRD and XPS experiments. At the Al Kα excitation energy of 1.487 keV used in XPS, $[Rh(COD)Cl]_2$ experiences a slightly higher dose than $[Ir(COD)Cl]_2$ since the mass absorption coefficient of the Rh catalyst at the Al Kα photon energy is greater than that of the Ir catalyst. The dose is therefore expected to be lower for the Ir catalyst than the Rh catalyst, which is indeed what is observed in the doses calculated from the relevant experimental parameters.
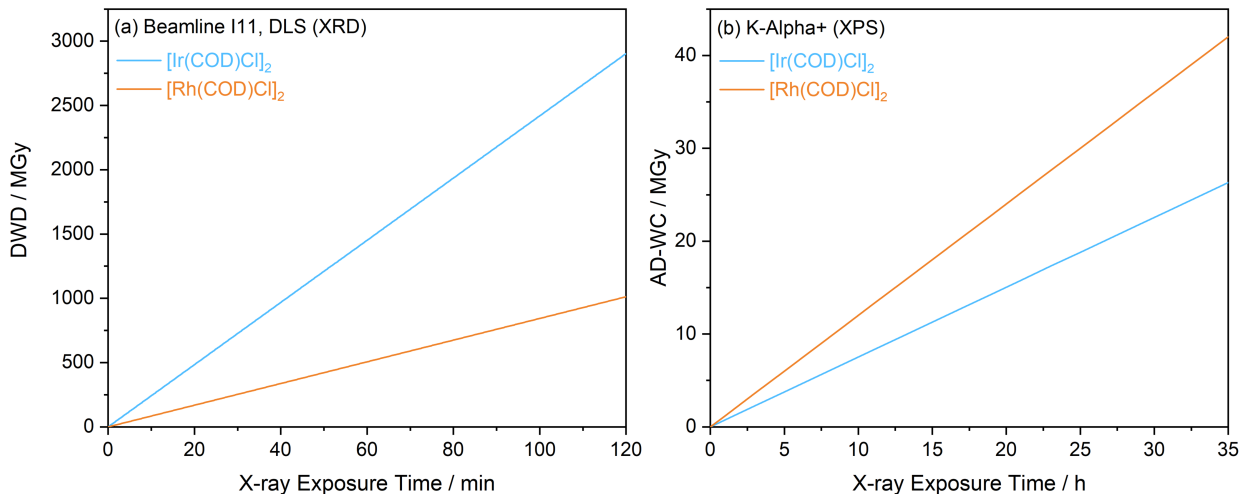

Figure 5: The linear dose – X-ray exposure time relationship for $[Ir(COD)Cl]_2$ and $[Rh(COD)Cl]_2$ for (a) PXRD using the Diffraction Weighted Dose (DWD) metric, and (b) XPS using the Average Dose Whole Crystal (AD-WC) metric. All dose calculations were performed using the small molecule feature in RADDOSE-3D.

The XP survey spectra for both catalysts are presented in Figure S12 of the Supplementary Information and show the expected M, Cl and C signals for both catalysts. High resolution core level spectra of the transition metals, as well as the Cl ligand, are shown in Figure 6. All core levels show significant changes with irradiation, including changes in peak intensity and position, as well as the appearance of additional features.

In order to analyse the core level spectra in more detail, a peak fitting analysis was performed. The initial Ir $4f$ spectrum of $[Ir(COD)Cl]_2$, collected during 0–1 h of X-ray
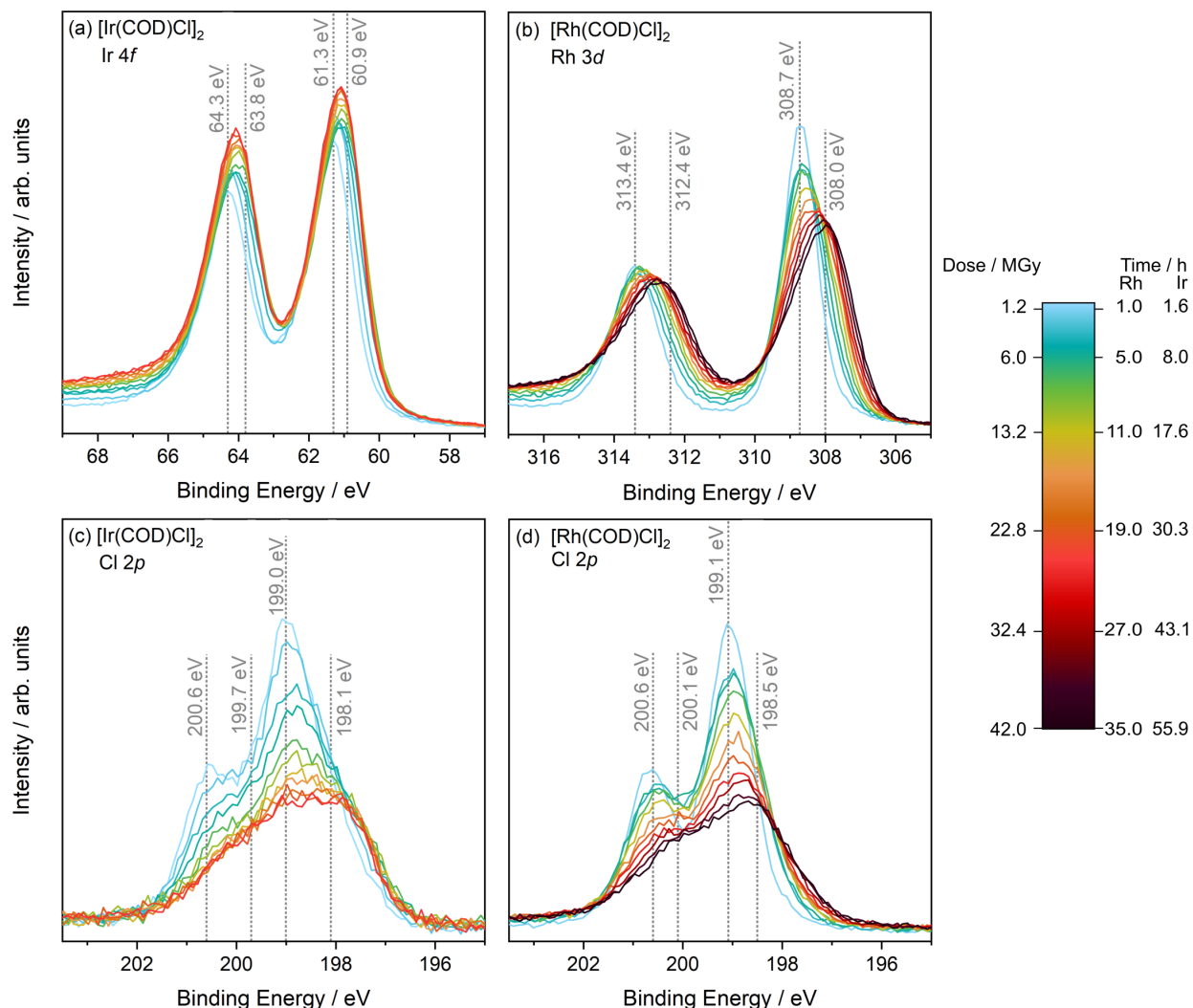
Figure 6: Core level X-ray photoelectron spectra of the $[M(COD)Cl]_2$ catalysts as a function of X-ray exposure, including (a) Ir $4f$ and (b) Rh $3d$ spectra of $[Ir(COD)Cl]_2$ and $[Rh(COD)Cl]_2$, respectively, and (c) and (d) Cl $2p$ spectra. The legend includes the measurement time as well as the calculated X-ray dose as Average Dose Whole Crystal (AD-WC) from RADDOSE-3D. The time given represents the end of each measurement period with each data acquisition approximately taking 1 h. For instance, 1 h on the plot corresponds to the measurement that began at t=0 h and finished at t=1 h. The grey dotted lines and binding energy values shown correspond to the binding energy positions of the main spectral contributions present in the first spectra (1 h).

irradiation and corresponding to a dose of 0.75 MGy, shows the presence of two chemical environments. The main contribution at 61.3 eV ($4f_{7/2}$) and 64.3 eV ($4f_{5/2}$) corresponds to the Ir^{+1} oxidation state of the molecule. As there are, to date, no published binding energies (BEs) of Ir $4f$ for this particular catalyst available, no direct comparison could be made with existing literature. However, these BEs are in good agreement with those for the Ir^{+1} $4f$ doublet found in the study of IrCl compounds by El-Issa *et al.*[78] In addition, Crotti *et al.* conducted photoelectron studies of multiple Ir COD catalysts of the chemical formula Ir(COD)(N–N)X, where N–N = 1,10-phenanthroline and its substituted derivatives.[79] For X=Cl, the Ir $4f_{7/2}$ BEs were reported to range from 61.17 eV to 61.44 eV for the various N-N forms investigated. These values correlate well with the experimental value of 61.3 eV found for the first iteration here.

In addition to the main feature of the core level clearly associated with Ir in the +1 oxidation state, a lower intensity feature is observed towards higher BE for the first iteration. This is associated with hydroxylated Ir surface species and this surface feature disappears after the second measurement group due to the irradiation induced desorption of the adsorbed surface species. More important for the understanding of radiation induced changes in [Ir(COD)Cl]$_2$ is the appearance of a feature on the lower BE side of the peaks, at 60.9 eV for $4f_{7/2}$ and 63.8 eV for Ir $4f_{5/2}$. This feature becomes more apparent with prolonged exposure time/absorbed dose. Previous studies of metallic Ir show the Ir $4f_{7/2}$ core level at BEs ranging from 60.1 eV to 60.8 eV.[80–82] Based on the observed intermediate BE of the feature found after increasing irradiation here, it can be attributed to a partial photoreduction and change of chemical environment of Ir.

The initial Rh $3d$ spectrum in [Rh(COD)Cl]$_2$ shows the presence of two chemical states. The main contribution at BEs of 308.7 eV ($3d_{5/2}$) and 313.4 eV ($3d_{3/2}$) agrees well with previously published BEs for Rh^{+1} of [Rh(COD)Cl]$_2$.[83–87] Peak fits of the asymmetric Rh $3d$ spectra reveal the presence of a low intensity doublet at lower BEs of 308.0 eV ($3d_{5/2}$) and 312.4 eV ($3d_{3/2}$). Previously reported Rh $3d_{5/2}$ BEs of metallic Rh are in the 307.0 eV to

307.4 eV range.[85,88] In parallel with the observations made for the Ir catalyst, this can be attributed to a partial photoreduction and change of chemical environment of Rh.

The Cl $2p$ core level spectra of both $[M(COD)Cl]_2$ catalysts are initially dominated by peaks at comparable BEs. The Cl $2p_{3/2}$ peaks lie at BEs of 199.0 eV (Ir) and 199.1 eV (Rh), and the Cl $2p_{1/2}$ peak is at BEs of 200.6 eV for both Ir and Rh. These BEs agree well with values presented in existing literature of Cl $2p$ in Ir and Rh halide compounds and coordination catalysts.[31,78,85,89] After the initial measurement period, both catalysts show a small Cl $2p_{3/2}$ contribution at lower BEs, at 198.1 eV and 198.5 eV, for Ir and Rh, respectively, corresponding to an additional Cl environment. This lower BE contribution increases gradually with increasing radiation dose, and can be explained by the breaking of M – Cl bonds, leading to Cl bound to a single metal centre, rather than in a bridging position. It is also noticeable that the overall spectral intensity of the Cl $2p$ core level decreases for both samples, which will be discussed in detail below. The C $1s$ core level spectra for both $[M(COD)Cl]_2$ catalysts show no notable change across the measurement duration (see Figure S13 in the Supplementary Information).

Beyond this qualitative discussion of changes to the BE features of the main core levels, quantitative changes could also be extracted from peak analysis (see Figure 7). Considering first the irradiation-induced changes to the metal core levels, both Ir $4f$ and Rh $3d$ spectra show a continuous increase in the intensity contributions of the lower BE components with irradiation time. In both metals a partial photoreduction from their original +1 oxidation state is observed from the onset of the measurements, and the quantitative changes in the ratio between the peaks associated with the +1 and reduced state are shown in Figure 7(a). Whilst the initial behaviour of both catalysts is comparable, the extent of the total reduction occurring varies between them. The relative atomic percentage (RAP) of Rh^{+1} reduces to 39.7% after a dose of 35 MGy, after which the spectra stabilise and no further reduction takes place. The Ir sample, however, stabilises after a dose of only 19 MGy at 63.3% RAP of Ir^{+1}. In parallel, the comparison of points of equivalent dose for the two catalysts is

insightful. For instance, at an absorbed dose of 25 MGy, equivalent to an irradiation time of 21 h for $[Rh(COD)Cl]_2$ and 33 h for $[Ir(COD)Cl]_2$, the RAP of Ir^{+1} relative to other chemical states present is 63.9%. This corresponds to a 37% decrease from the starting value. At the same dose, $[Rh(COD)Cl]_2$ is found to have a Rh^{+1} RAP of 48.7%, corresponding to a 38% decrease from the starting value of the first measurement iteration. These observations indicate that during XPS experiments, $[Rh(COD)Cl]_2$ has close to equivalent, if not, slightly greater susceptibility to X-ray induced chemical environment changes than $[Ir(COD)Cl]_2$.

Notable changes are also observed in the Cl $2p$ spectra with increasing dose. In both $[M(COD)Cl]_2$ catalysts, besides the change in BE noted above, the total Cl signal intensity reduces drastically with increasing dose. Figure 7(c) shows the Cl to M ratios with irradiation time and dose. The Rh catalyst experiences a total Cl loss of 14% and the Ir catalyst a loss of 21% over the total measurement period. This loss of Cl indicates a cleaving of the M – Cl bonds of the central rhombus structure, which can result in the formation of free chlorine species, which are lost to vacuum in the XPS measurements. The loss of Cl for both catalysts continues past the dose at which the reduction of the corresponding metal centres ceases, most likely suggesting a multi-step process of cleaving only one or both M – Cl bonds. At a dose of 25 MGy the Ir catalyst undergoes a 20.7% loss in Cl intensity compared to a 9.9% Cl loss in the Rh catalyst. In addition to the clear loss in Cl experienced by both samples with increasing dose, there is a simultaneous growth in contribution of the lower BE Cl environment, most likely from bridging Cl atoms that have lost one M – Cl bond and are only bound to a single metal atom (see Figure 7(d)). These observations point to a complex change in the M – Cl environment, including the cleaving of bonds, the loss of Cl, and the formation of new M and Cl environments. This result, combined with the observed oxidation state reduction noted above, gives an overall picture of the chemical environment changes taking place during irradiation of the samples. Whilst the extent of Ir photoreduction is lower than that of Rh, if not equivalent, the loss of Cl in Ir is almost double that of Rh at equivalent dose. This is an indication that despite the metal centres having similar stabilities,
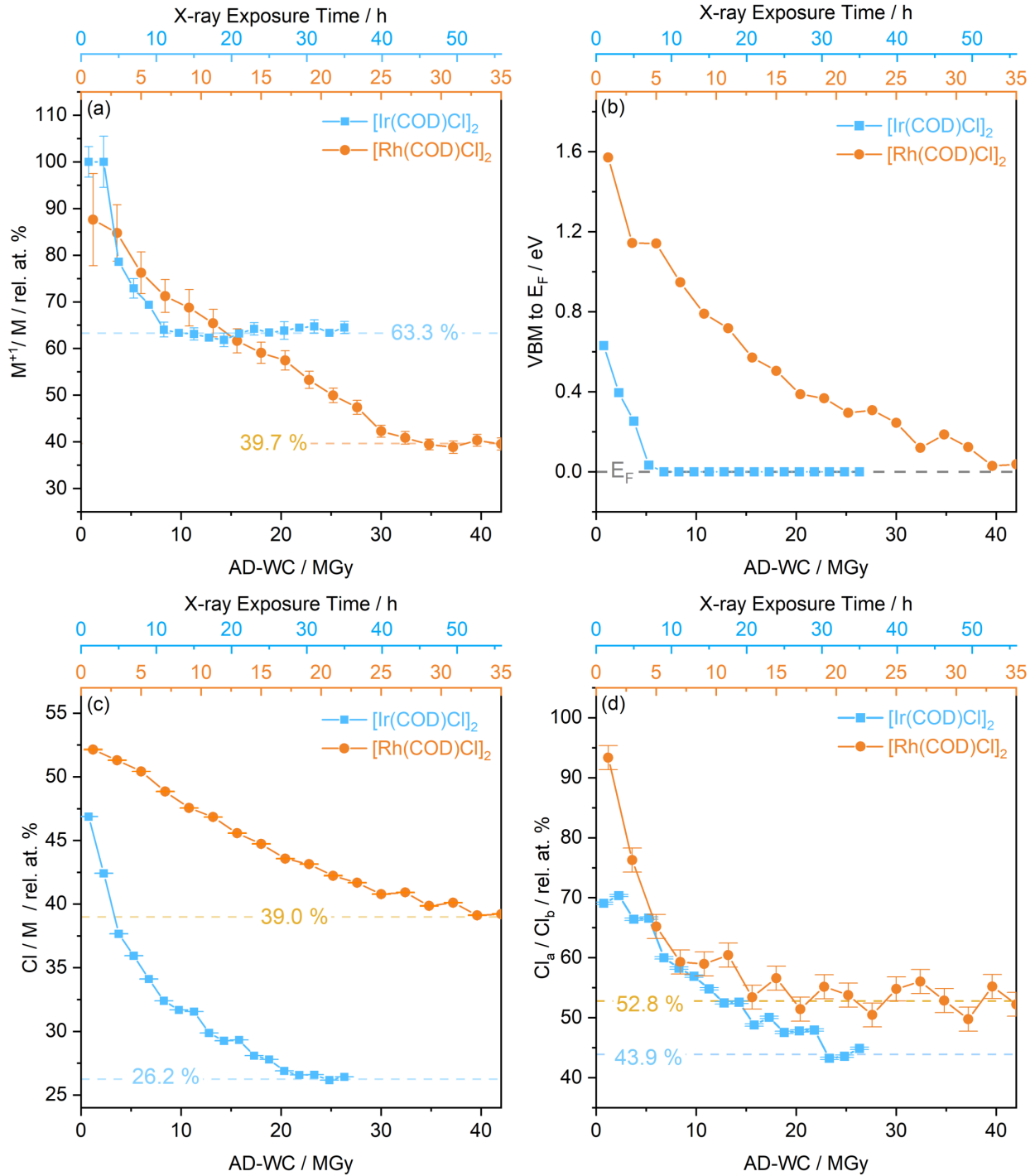
Figure 7: Quantitative changes to photoelectron spectra as a function of dose and X-ray exposure time extracted from core level and valence state analysis. (a) Relative atomic percentages (RAPs) (rel. at. % in plot) of the ratios of the Ir and Rh core level contributions. (b) Distance between VBM and E_F. (c) RAP ratios of the total M and Cl signals. (d) RAPS of the ratios of the two Cl environments observed, where Cl_a is the main Cl environment and Cl_b is the additional, lower BE feature.

the Ir – Cl bond of the Ir catalyst lacks the integrity of the Rh – Cl bond of [Rh(COD)Cl]$_2$.

The radiation induced changes to both the structure and the local chemical environments manifest themselves in changes to the electronic structure. Figures 8(a) and (b) show the XPS valence band spectra of the [M(COD)Cl]$_2$ catalysts. A clear increase in intensity at the valence band maximum (VBM) with dose, resulting in the narrowing of the VBM to Fermi energy (E_F) separation, occurs. This goes hand in hand with the photoreduction of the metal centres observed in the core levels and the resulting increase in carrier concentration. Figure 7(b) shows the VBM position of the [M(COD)Cl]$_2$ catalysts relative to the E_F at 0 eV, which was determined by taking the intercept of the linear fit of the VBM slope with the linear fit of the background at the lower BE side. In agreement with the photoreduction and subsequent stabilisation of the Rh oxidation states in the [Rh(COD)Cl]$_2$ core level spectra, the VBM position also stabilises in the last few measurement points. For the Ir catalyst, initially a large decrease in the VBM position is observed, and after a dose of 6.8 MGy the band gap closes and the system becomes effectively metallic. Therefore, after this point the VBM position is equivalent to E_F at 0 eV.

Beyond the quantitative evaluation of the VBM position and the clear correlation to the observed photoreduction, densities of states (DOS) from DFT calculations are needed to further interpret the valence electronic structure of the catalysts. The crystal structures obtained from the Rietveld refinement of the initial PXRD measurements of both catalysts were used as the starting point for the calculations. Table 3 summarises the experimental unit cell parameters for both the first and last PXRD iteration as well as the theoretical unit cell parameters after relaxation. The differences between experiment and relaxed theory structures, also included in the Table, are small for both catalysts. The unweighted total and projected DOS calculated using DFT based on the relaxed structures are shown in Figure S16 in the Supplementary Information. In order to compare the PDOS to the valence band spectra from XPS, they were weighted using one-electron photoionisation cross sections as outlined in the methods section.
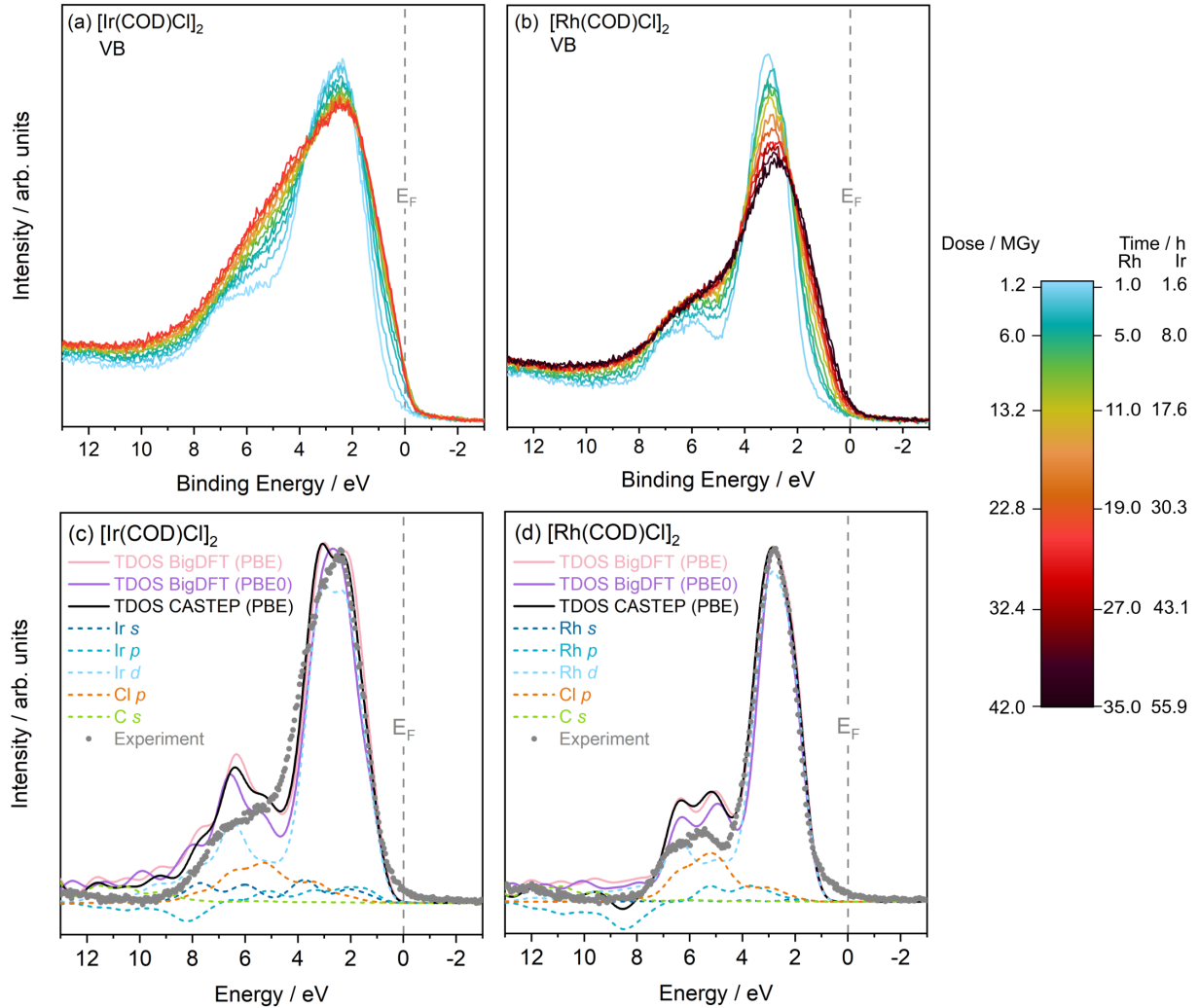
Figure 8: Electronic structure of the $[M(COD)Cl]_2$ catalysts. (a) and (b) Valence band X-ray photoelectron spectra of $[Ir(COD)Cl]_2$ and $[Rh(COD)Cl]_2$, respectively. The legend includes the measurement time as well as the calculated X-ray dose as Average Dose Whole Crystal (AD-WC) from RADDOSE-3D. (c) and (d) Broadened and photoionisation cross section corrected total (TDOS) and projected (PDOS) density of states, calculated using the CASTEP code with the PBE functional, compared to the initial XPS data for $[Ir(COD)Cl]_2$ and $[Rh(COD)Cl]_2$, respectively. Only the states with significant contributions to the intensity are displayed. The TDOS is included for both the CASTEP PBE calculations as well as for the BigDFT PBE and PBE0 calculations for comparison. The Fermi energy E_F at 0 eV is indicated in all subfigures.

The CASTEP PDOS calculations rely on the projection onto a Linear Combination of Atomic Orbitals (LCAO) basis set,[90] a process which can be sensitive to both the simulation parameters and the choice of LCAO basis set. Although the charge spilling parameter is low (less than 1 %) for both systems, indicating that the LCAO basis is sufficient to represent the system, negative contributions are present for both Rh and Ir p states. These features were found to be insensitive to simulation parameters, including the choice of pseudopotential, cut-off energy, and k-point sampling. To further assess the quality of the projection, additional calculations for gas phase molecules using the BigDFT code were therefore performed, for which results are presented in Figure S16 in the Supplementary Information. The BigDFT calculations do not have any significant negative contributions. However, despite the use of differing basis sets between the two codes, the PDOS are otherwise very similar, particularly in the region closest to the VB edge. This indicates that the intermolecular interactions have a relatively small impact. In addition, the effect of the functional was investigated by performing PBE0 calculations in BigDFT. The differences with respect to PBE are more significant than between BigDFT and CASTEP PBE calculations, with the differences becoming more pronounced the further from the VBM, where the peaks become more spread out for PBE0. Nonetheless, the PDOS remain qualitatively similar.

Figures 8(c) and (d) show a direct comparison of the weighted PDOS with the XPS spectra for both [M(COD)Cl]$_2$ catalysts, showing that DFT is able to describe both the individual features as well as their relative energy positions very well. As with the unweighted PDOS, the differences between CASTEP and BigDFT spectra are small, with the key differences arising due to the negative contributions in CASTEP, while the differences between PBE0 and PBE are more pronounced. For both systems there are some differences in relative peak heights, while for [Ir(COD)Cl]$_2$ the splitting in the peak at the VBM disappears for PBE0. Nonetheless, the key features are similar. Notably, for both systems and irrespective of the level of theory, the top of the valence band is dominated by metal d states with some hybridisation from metal s and p states. This directly explains the intensity increase observed

29

in this region upon irradiation due to the photoreduction of the metal centres. In addition to influencing the metal states at the top of the valence band, this also results in an increase in intensity across the 4–8 eV region. In this energy range strong contributions from the metal states are still prevalent, in addition to larger hybridisation with Cl p states. Although Cl is lost in both catalysts with irradiation, the increase in electron density for the metals dominates.

Table 3: Unit cell parameters obtained from the Rietveld refinement of the first ($\mathrm{PXRD_{start}}$) and final ($\mathrm{PXRD_{end}}$) PXRD data and from DFT calculations for $\mathrm{[Ir(COD)Cl]_2}$ and $\mathrm{[Rh(COD)Cl]_2}$. a, b, and c are the lattice parameters, α, β, and γ are the unit cell angles, and V is the unit cell volume. The percentage difference ($\Delta\%$) between the first experimental and theoretical values is also included.

Compound		a / Å	b / Å	c / Å	α / °	β / °	γ / °	V / Å^3
	DFT	14.840	13.771	16.111	90.000	90.001	90.002	3292.470
$\mathrm{[Ir(COD)Cl]_2}$	$\mathrm{PXRD_{start}}$	15.1775(1)	13.6407(1)	16.3046(2)	90.000	90.000	90.000	3375.56
	$\mathrm{PXRD_{end}}$	15.2883(5)	13.7562(5)	16.3408(6)	90.000	90.000	90.000	3436.62
	$\Delta\%$	-2.220	0.953	-1.190	0.000	0.001	0.003	-2.462
	DFT	7.170	25.239	8.865	90.000	90.976	90.000	1604.010
$\mathrm{[Rh(COD)Cl]_2}$	$\mathrm{PXRD_{start}}$	7.3008(1)	25.4525(4)	9.0482(1)	90.000	91.877(1)	90.000	1680.46
	$\mathrm{PXRD_{end}}$	7.3011(1)	25.4869(5)	9.0642(2)	90.000	91.988(1)	90.000	1685.67
	$\Delta\%$	-1.781	-0.839	-2.025	0.000	-0.981	0.000	-4.549

31

Combining the observations made in PXRD and XPS, a comprehensive picture of the radiation-induced changes in both catalysts emerges. Dose calculations enable comparisons of the effects of sample irradiation between techniques, and show that the full 35 h, 18 iteration, XPS experiment on $[Ir(COD)Cl]_2$ results in an absorbed X-ray dose of 26.3 MGy, which is approximately the same as 1 min for the PXRD experiment. The data presented here provides further evidence that established strategies to mitigate radiation damage, such as reduction in measurement times, are effective. More importantly however, the results presented here highlight the significant influence of differences in experimental setups and parameters used. These vary not only between different techniques, but also between different systems and beamlines, strongly influencing the absorbed dose and consequently the extent of X-ray-induced sample change. Furthermore, the crucial difference in sample environments between XRD and XPS must be recognised. PXRD experiments are conducted under ambient conditions, whereas XPS is performed under ultra-high vacuum (UHV) conditions. Under UHV conditions the loss of Cl in particular may be enhanced, whilst the presence of air, and its ionisation through X-rays, may lead to additional reaction pathways of e.g. H_2O and O_2 with the catalysts.[91,92] Whilst it is beyond the scope of the current manuscript to explore these aspects in detail, this is certainly an interesting aspect to consider in future experiments. However, although the environmental differences are important, some clear conclusions emerge from the combination of the two experimental techniques and DFT. PXRD experiments show significant structural changes (i.e. to the unit cell and atomic positions) in the Ir catalyst compared to more subtle changes in the Rh catalyst. XPS analysis shows that increasing X-ray irradiation appears to have a similar effect on the reduction of the metals as determined from the quantification of peak fits. The loss of Cl at the same dose of 1012 MGy, however, is 10% greater for Ir than it is for Rh. From Rietveld refinements of the PXRD data it is clear that the decreasing Cl – Cl distance, is giving rise to a global extension of the M – Cl bond. XPS is able to explain this global increase in bond length through the observation of local loss of bridging Cl atoms as well as the overall loss of Cl

from the system. Whilst PXRD is invaluable for determining global structural information, a crucial aspect not observable is the photoreduction of the metal centres clearly visible in both core and valence XP spectra. DFT calculations enable the interpretation of observed changes to the valence state in detail and help to pinpoint metal contributions.

Conclusions

This work presents a systematic, multi-technique approach to explore and understand X-ray induced effects on the structure, chemical environments, and electronic structure of Ir and Rh centered $[M(COD)Cl]_2$ catalysts. Iterative synchrotron PXRD and laboratory XPS experiments are successfully combined with DFT calculations, and radiation dose calculations enable the comparison between different experimental setups and samples. For the first time dose calculations are applied to photoelectron spectroscopy experiments.

PXRD shows global structural changes with increasing radiation dose as bond angle and interatomic distance changes, as well as a gradual increase in unit cell volume. The significant changes in $[Ir(COD)Cl]_2$ relative to $[Rh(COD)Cl]_2$ at the same absorbed dose point to the intrinsic instability of the sample and structural robustness of $[Rh(COD)Cl]_2$ upon irradiation. XPS reveals that neither $[Ir(COD)Cl]_2$ nor $[Rh(COD)Cl]_2$ are chemically and electronically stable under the experimental conditions. Both are found to undergo a drastic change and loss in Cl environments, Ir to a greater extent than Rh, pointing to a more robust $Rh^{+1} - Cl$ bond than the Ir^{+1} equivalent. Comparable levels of photoreduction of the metal centres are observed in both catalysts, albeit marginally greater for Rh than Ir, demonstrating similar stabilities of the respective M^{+1} oxidation states. Changes to the valence states of both catalysts are understood by direct comparison with PDOS from DFT calculations, further underlining the effects of photoreduction, including a narrowing of the VBM to E_F distance.

The combination of complimentary techniques used in this work, namely XRD, XPS

and DFT, is shown to be invaluable for determining the sample stability and behaviour under irradiation by enabling the direct correlation of global structural changes with local electronic and chemical effects. In order to draw meaningful comparisons across these X-ray techniques, robust X-ray dose estimates depend on the knowledge of the experimental parameters during measurement, including the beam energy, flux, size and profile. This study of two prototypical catalysts establishes a suitable and robust approach to understanding irradiation-induced effects in small molecular crystals. The results provide new insights into the fundamental stability of metalorganic complexes, which could be invaluable for future work on damage mitigation strategies. This work paves the way for systematic investigations into X-ray induced changes in a wide range of small molecular systems important to many technological applications.

Acknowledgement

Supporting Information Available

The unit cell parameters obtained from the refinement of SCXRD data collected at 300 K at beamline I19 at Diamond Light Source, of $[Ir(COD)Cl]_2$ and $[Rh(COD)Cl]_2$. The ORTEP diagrams of the structure of the Ir and Rh catalysts from SCXRD analysis. The diffraction weighted dose as a function of X-ray exposure time for the Ir and Rh catalysts during PXRD at beamline I11, and SCXRD at beamline I19 at Diamond Light Source. The Rietveld refinements of the first and last Ir and Rh PXRD patterns are also included. A figure of the $[Ir(COD)Cl]_2$ peak area, determined by Le Bail refinements with respect to the beam current fluctuations caused by electron top-up of the beamline. The change in the β lattice parameter of the Rh catalyst, obtained from Le Bail refinements, over 1012 MGy dose (2 h of irradiation). A plot of the Rietveld refinement of the last Ir PXRD pattern in which the space group was permitted to transform into a monoclinic $P2_1/n$ phase, using the ISODISTORT online utility. The change in the β lattice parameter obtained from Rietveld refinements, allowing the Ir catalyst to transition to a monoclinic phase. X-ray photoelectron spectra of the survey scans of Ir and Rh catalysts, along with the C $1s$ spectra for both catalysts with increasing dose. The shift in the Rh $3d$, Cl $2p$ and C $1s$ core level spectra observed for the Rh catalyst, between the first and second measurement iterations, are presented. Peak fits of the X-ray photoelectron core level spectra at a dose of 15.8 MGy for Ir and Rh catalysts. The unweighted total (TDOS) and projected density of states (PDOS), calculated using density functional theory, using the BigDFT code and PBE functional, BigDFT with the PBE0 functional and CASTEP with the PBE functional. The weighted total (TDOS) and projected density of states (PDOS), calculated using the BigDFT code with the PBE functional, BigDFT with the PBE0 functional, and CASTEP with the PBE functional for $[Ir(COD)Cl]_2$ and $[Rh(COD)Cl]_2$. The theoretical data are aligned to the experimental VB for comparison. A comparative plot of the unweighted and weighted total projected density of states (TDOS), calculated using the two different codes and functionals for both catalysts. A discussion of RADDOSE-3D, with the input parameters used in the estimation of X-ray

dose for the XRD and XPS experiments, is provided.

References

(1) Holton, J. M. A beginner's guide to radiation damage. *Journal of Synchrotron Radiation* **2009**, *16*, 133–142.

(2) Garman, E. F. Radiation damage in macromolecular crystallography: what is it and why should we care? *Acta Crystallographica Section D Biological Crystallography* **2010**, *66*, 339–351.

(3) Taberman, H. Radiation Damage in Macromolecular Crystallography—An Experimentalist's View. *Crystals* **2018**, *8*, 157.

(4) Garman, E. F.; Weik, M. *Protein Crystallography. Methods in Molecular Biology*; Humana Press: New York, 2017; Chapter 20, pp 467–489.

(5) Abrahams, S. C. International Union of Crystallography Commission on Crystallographic Apparatus Single-Crystal Radiation Damage Study. *Acta Crystallographica Section A* **1973**, *29*, 111–116.

(6) Seiler, P.; Dunitz, J. D. Detection of Radiation Damage in Organic Crystals. *Australian Journal of Physics* **1985**, *38*, 405–411.

(7) Christensen, J.; Horton, P. N.; Bury, C. S.; Dickerson, J. L.; Taberman, H.; Garman, E. F.; Coles, S. J. Radiation damage in small-molecule crystallography: fact not fiction. *IUCrJ* **2019**, *6*, 703–713.

(8) Coates, C. S.; Murray, C. A.; Boström, H. L. B.; Reynolds, E. M.; Goodwin, A. L. Negative X-ray expansion in cadmium cyanide. *Materials Horizons* **2021**,

(9) Morgan, L. C.; Kim, Y.; Blandy, J. N.; Murray, C. A.; Christensen, K. E.; Thompson, A. L. Unexpected behaviour in derivatives of Barluenga's reagent, Hal(Coll)2X (Coll = 2,4,6-trimethyl pyridine, collidine; Hal = I, Br; X = PF6, ClO4& BF4). *Chemical Communications* **2018**, *54*, 9849–9852.

(10) Clegg, W. *X-ray Crystallography*, 2nd ed.; Oxford University Press, 2015; Chapter 1, pp 11–31.

(11) Hemberg, O.; Otendal, M.; Hertz, H. M. Liquid-metal-jet anode electron-impact X-ray source. *Applied Physics Letters* **2003**, *83*, 1483–1485.

(12) Skarzynski, T. Collecting data in the home laboratory: evolution of X-ray sources, detectors and working practices. *Acta Crystallographica Section D Biological Crystallography* **2013**, *69*, 1283–1288.

(13) Hornberger, B.; Kasahara, J.; Gifford, M.; Ruth, R.; Loewen, R. A compact light source providing high-flux, quasi-monochromatic, tunable X-rays in the laboratory. Advances in Laboratory-based X-Ray Sources, Optics, and Applications VII. 2019; pp 1 – 13.

(14) Gadjev, I.; Sudar, N.; Babzien, M.; Duris, J.; Hoang, P.; Fedurin, M.; Kusche, K.; Malone, R.; Musumeci, P.; Palmer, M. et al. An inverse free electron laser acceleration-driven Compton scattering X-ray source. *Scientific Reports* **2019**, *9*, 532.

(15) Tavares, P. F.; Al-Dmour, E.; Andersson, Å.; Cullinan, F.; Jensen, B. N.; Olsson, D.; Olsson, D. K.; Sjöström, M.; Tarawneh, H.; Thorin, S. et al. Commissioning and first-year operational results of the MAX IV 3 GeV ring. *Journal of Synchrotron Radiation* **2018**, *25*, 1291–1316.

(16) Liu, L.; Milas, N.; Mukai, A. H. C.; Resende, X. R.; de Sá, F. H. The Sirius project. *Journal of Synchrotron Radiation* **2014**, *21*, 904–911.

(17) Raimondi, P. ESRF-EBS: The Extremely Brilliant Source Project. *Synchrotron Radiation News* **2016**, *29*, 8–15.

(18) Alekou, A.; Bartolini, R.; Carmignani, N.; Liuzzo, S. M.; Raimondi, P.; Pulampong, T.; Walker, R. P. Novel Double Triple Bend Achromat (DTBA) lattice design for a next generation 3 GeV Synchrotron Light Source. *arXiv* **2018**, 1801.02522v2 [physics.acc–ph].

(19) Martin, I. P. S.; Bartolini, R. Conceptual design of an accumulator ring for the Diamond II upgrade. *Journal of Physics: Conference Series* **2018**, *1067*, 032005.

(20) Wright, J.; Giacobbe, C.; Majkut, M. New opportunities at the Materials Science Beamline at ESRF to exploit high energy nano-focus X-ray beams. *Current Opinion in Solid State and Materials Science* **2020**, *24*, 100818.

(21) Altarelli, M. The European X-ray Free-Electron Laser: toward an ultra-bright, high repetition-rate X-ray source. *High Power Laser Science and Engineering* **2015**, *3*, e18.

(22) Henderson, R. Cryo-protection of protein crystals against radiation damage in electron and X-ray diffraction. *Proceedings of the Royal Society of London. Series B: Biological Sciences* **1990**, *241*, 6–8.

(23) Gonzalez, A.; Thompson, A. W.; Nave, C. Cryo-protection of protein crystals in intense x-ray beams. *Review of Scientific Instruments* **1992**, *63*, 1177–1180.

(24) Teng, T.-Y.; Moffat, K. Radiation damage of protein crystals at cryogenic temperatures between 40 K and 150 K. *Journal of Synchrotron Radiation* **2002**, *9*, 198–201.

(25) Murray, J.; Garman, E. Investigation of possible free-radical scavengers and metrics for radiation damage in protein cryocrystallography. *Journal of Synchrotron Radiation* **2002**, *9*, 347–354.

(26) Garman, E. 'Cool' crystals: macromolecular cryocrystallography and radiation damage. *Current Opinion in Structural Biology* **2003**, *13*, 545–551.

(27) Zeldin, O. B.; Gerstel, M.; Garman, E. F. RADDOSE-3D : time- and space-resolved modelling of dose in macromolecular crystallography. *Journal of Applied Crystallography* **2013**, *46*, 1225–1230.

(28) Bury, C. S.; Brooks-Bartlett, J. C.; Walsh, S. P.; Garman, E. F. Estimate your dose: RADDOSE-3D. *Protein Science* **2018**, *27*, 217–228.

(29) Brooks-Bartlett, J. C.; Batters, R. A.; Bury, C. S.; Lowe, E. D.; Ginn, H. M.; Round, A.; Garman, E. F. Development of tools to automate quantitative analysis of radiation damage in SAXS experiments. *Journal of Synchrotron Radiation* **2017**, *24*, 63–72.

(30) Dickerson, J. L.; McCubbin, P. T. N.; Garman, E. F. RADDOSE-XFEL : femtosecond time-resolved dose estimates for macromolecular X-ray free-electron laser experiments. *Journal of Applied Crystallography* **2020**, *53*, 549–560.

(31) Mason, R.; Mingos, D. M. P.; Rucci, G.; Connor, J. A. Electron emission spectroscopic studies of olefin and other complexes of d^8 and d^{10} metal ions. *Journal of the Chemical Society, Dalton Transactions* **1972**, *16*, 1729–1731.

(32) Westcott, S. A.; Parthasarathy, S.; Gildner, P. G.; Colacot, T. J. *Encyclopedia of Reagents for Organic Synthesis*; John Wiley & Sons, Ltd: Chichester, UK, 2018.

(33) Hesp, K. D.; Stradiotto, M. Intramolecular Hydroamination of Unactivated Alkenes with Secondary Alkyl- and Arylamines Employing [Ir(COD)Cl]$_2$ as a Catalyst Precursor. *Organic Letters* **2009**, *11*, 1449–1452.

(34) Crabtree, R. H.; Morehouse, S. M.; Quirk, J. M. [η 4 -1,5-Cyclooctadiene)(Pyridine)-(Tricyclohexylphosphine)Iridium(I)Hexafluorophosphate. *Inorganic Syntheses* **2007**, *24*, 173–176.

(35) Ashfeld, B. L.; Judd, A. S. *Encyclopedia of Reagents for Organic Synthesis*; John Wiley & Sons, Ltd: Chichester, 2007.

(36) Cotton, F. A.; Lahuerta, P.; Sanau, M.; Schwotzer, W. Air oxidation of $Ir_2(Cl)_2(COD)_2$ revisited. The structures of $[Ir(\mu_2\text{-}Cl)(COD)]_2$(ruby form) and its oxidation product, $Ir_2Cl_2(COD)_2(\mu_2\text{-}OH)_2(\mu_2\text{-}O)$. *Inorganica Chimica Acta* **1986**, *120*, 153–157.

(37) Tabrizi, D.; Manoli, J.; Dereigne, A. Etude radiocristallographique de μ-dichloro-bis (π cyclooctadiène-1,5) diiridium: $[(COD-1,5)\,IrCl]_2$, variété jaune-orange. *Journal of the Less Common Metals* **1970**, *21*, 337–339.

(38) Pannetier, G.; Tabrizi, D. Etude radiocristallographique du di-μ-chloro-bis (π-cyclooctadiène-1,5) diiridium $[(COD-1,5)\,lrCl]_2$, variété orthorhombique (rouge-rubis). *Journal of the Less Common Metals* **1971**, *23*, 110–112.

(39) Berger, M.; Hubbell, J.; Seltzer, S.; Chang, J.; Coursey, J.; Sukumar, R.; Zucker, D.; Olsen, K. XCOM: Photon Cross Section Database (version 1.5). 2010; `http://physics.nist.gov/xcom`.

(40) Thompson, S. P.; Parker, J. E.; Potter, J.; Hill, T. P.; Birt, A.; Cobb, T. M.; Yuan, F.; Tang, C. C. Beamline I11 at Diamond: A new instrument for high resolution powder diffraction. *Review of Scientific Instruments* **2009**, *80*, 075107.

(41) Thompson, S. P.; Parker, J. E.; Marchal, J.; Potter, J.; Birt, A.; Yuan, F.; Fearn, R. D.; Lennie, A. R.; Street, S. R.; Tang, C. C. Fast X-ray powder diffraction on I11 at Diamond. *Journal of Synchrotron Radiation* **2011**, *18*, 637–648.

(42) Coelho, A. A. TOPAS and TOPAS-Academic : an optimization program integrating computer algebra and crystallographic objects written in C++. *Journal of Applied Crystallography* **2018**, *51*, 210–218.

(43) Coelho, A. A. Coelho Software, Brisbane.

(44) Nowell, H.; Barnett, S. A.; Christensen, K. E.; Teat, S. J.; Allan, D. R. I19, the small-molecule single-crystal diffraction beamline at Diamond Light Source. *Journal of Synchrotron Radiation* **2012**, *19*, 435–441.

(45) Oxford Diffraction /Agilent Technologies UK Ltd, CrysAlisPRO.

(46) Dolomanov, O. V.; Bourhis, L. J.; Gildea, R. J.; Howard, J. A. K.; Puschmann, H. OLEX2 : a complete structure solution, refinement and analysis program. *Journal of Applied Crystallography* **2009**, *42*, 339–341.

(47) Watts, J. F.; Wolstenholme, J. *An Introduction to Surface Analysis by XPS and AES*, 2nd ed.; John Wiley & Sons, 2019; Chapter 3, p 93.

(48) NIST X-ray Photoelectron Spectroscopy Database, NIST Standard Reference Database Number 20, National Institute of Standards and Technology, Gaithersburg MD, 20899 (2000), doi:10.18434/T4T88K, (retrieved 26-02-2021).

(49) Rogers, J. D.; Sundaram, V. S.; Kleiman, G. G.; Castro, S. G. C.; Douglas, R. A.; Peter-levitz, A. C. High resolution study of the $M_{45}N_{67}N_{67}$ and $M_{45}N_{45}N_{67}$ Auger transitions in the 5d series. *Journal of Physics F: Metal Physics* **1982**, *12*, 2097–2102.

(50) Wittmer, M.; Oelhafen, P.; Tu, K. N. Electronic structure of iridium silicides. *Physical Review B* **1986**, *33*, 5391–5400.

(51) van der Heide, P. *X-Ray Photoelectron Spectroscopy*; John Wiley & Sons, Inc.: Hoboken, NJ, USA, 2011; pp 171–176.

(52) Sesselmann, W.; Chuang, T. The interaction of chlorine with copper. *Surface Science* **1986**, *176*, 67–90.

(53) Zeldin, O. B.; Brockhauser, S.; Bremridge, J.; Holton, J. M.; Garman, E. F. Predicting the X-ray lifetime of protein crystals. *Proceedings of the National Academy of Sciences* **2013**, *110*, 20551–20556.

(54) Paithankar, K. S.; Owen, R. L.; Garman, E. F. Absorbed dose calculations for macro-molecular crystals: improvements to RADDOSE. *Journal of Synchrotron Radiation* **2009**, *16*, 152–162.

(55) Paithankar, K. S.; Owen, R. L.; Garman, E. F. Absorbed dose calculations for macro-molecular crystals: improvements to *RADDOSE*. Erratum. *Journal of Synchrotron Radiation* **2018**, *25*, 627–628.

(56) Storm, L.; Israel, H. I. Photon cross sections from 1 keV to 100 MeV for elements Z=1 to Z=100. *Atomic Data and Nuclear Data Tables* **1970**, *7*, 565–681.

(57) Hohenberg, P.; Kohn, W. Inhomogeneous Electron Gas. *Physical Review* **1964**, *136*, B864–B871.

(58) Kohn, W.; Sham, L. J. Self-Consistent Equations Including Exchange and Correlation Effects. *Physical Review* **1965**, *140*, A1133–A1138.

(59) Clark, S. J.; Segall, M. D.; Pickard, C. J.; Hasnip, P. J.; Probert, M. J.; Refson, K.; Payne, M. First principles methods using CASTEP. *Zeitschrift für Kristallographie* **2005**, *220*, 567–570.

(60) Perdew, J. P.; Burke, K.; Ernzerhof, M. Generalized gradient approximation made simple. *Physical Review Letters* **1996**, *77*, 3865–3868.

(61) Monkhorst, H. J.; Pack, J. D. Special points for Brillouin-zone integrations. *Physical Review B* **1976**, *13*, 5188–5192.

(62) Tkatchenko, A.; Scheffler, M. Accurate Molecular Van Der Waals Interactions from Ground-State Electron Density and Free-Atom Reference Data. *Physical Review Letters* **2009**, *102*, 073005.

(63) Ratcliff, L. E.; Dawson, W.; Fisicaro, G.; Caliste, D.; Mohr, S.; Degomme, A.; Videau, B.; Cristiglio, V.; Stella, M.; D'Alessandro, M. et al. Flexibilities of wavelets as

a computational basis set for large-scale electronic structure calculations. *The Journal of Chemical Physics* **2020**, *152*, 194110.

(64) Adamo, C.; Barone, V. Toward reliable density functional methods without adjustable parameters: The PBE0 model. *The Journal of Chemical Physics* **1999**, *110*, 6158–6170.

(65) Goedecker, S.; Teter, M.; Hutter, J. Separable dual-space Gaussian pseudopotentials. *Physical Review B* **1996**, *54*, 1703–1710.

(66) Hartwigsen, C.; Goedecker, S.; Hutter, J. Relativistic separable dual-space Gaussian pseudopotentials from H to Rn. *Physical Reiew B* **1998**, *58*, 3641–3662.

(67) Mulliken, R. S. Electronic Population Analysis on LCAO–MO Molecular Wave Functions. I. *The Journal of Chemical Physics* **1955**, *23*, 1833–1840.

(68) Morris, A. J.; Nicholls, R. J.; Pickard, C. J.; Yates, J. R. OptaDOS: A tool for obtaining density of states, core-level and optical spectra from electronic structure codes. *Computer Physics Communications* **2014**, *185*, 1477–1485.

(69) Scofield, J. H. *Theoretical Photoionization Cross Sections from 1 to 1500 keV*; 1973.

(70) Kalha, C.; Fernando, N. K.; Regoutz, A. Digitisation of Scofield Photoionisation Cross Section Tabulated Data. 2020.

(71) Jackson, A. J.; Ganose, A. M.; Regoutz, A.; Egdell, R. G.; Scanlon, D. O. Galore: Broadening and weighting for simulation of photoelectron spectroscopy. *Journal of Open Source Software* **2018**, *3*, 773.

(72) Bismuto, A.; Trapp, N.; Morandi, B. CCDC 1913379: Experimental Crystal Structure Determination. 2019.

(73) Hill, T. N. CCDC 1477153: Experimental Crystal Structure Determination. 2016.

(74) Zavalij, P. Y.; Stevens, L. M.; Eichhorn, B. W. CCDC 1920502: Experimental Crystal Structure Determination. 2019.

(75) Campbell, B. J.; Stokes, H. T.; Tanner, D. E.; Hatch, D. M. ISODISPLACE : a web-based tool for exploring structural distortions. *Journal of Applied Crystallography* **2006**, *39*, 607–614.

(76) Stokes, H. T.; Campbell, B. J.; Hatch, D. M. ISODISTORT, ISOTROPY Software Suite. 2020; `iso.byu.edu`.

(77) Bearden, J. A.; Burr, A. F. Reevaluation of X-ray atomic energy levels. *Reviews of Modern Physics* **1967**, *39*, 125–142.

(78) El-Issa, B. D.; Katrib, A.; Ghodsian, R.; Salsa', B. A.; Addassi, S. H. A comparative study of the bonding in different halides of iridium. *International Journal of Quantum Chemistry* **1988**, *33*, 195–216.

(79) Crotti, C.; Farnetti, E.; Filipuzzi, S.; Stener, M.; Zangrando, E.; Moras, P. Evaluation of the donor ability of phenanthrolines in iridium complexes by means of synchrotron radiation photoemission spectroscopy and DFT calculations. *Dalton Trans.* **2007**, 133–142.

(80) Escard, J.; Pontvianne, B.; Contour, J. Etude par spectroscopie de photoelectrons des interactions metal—support dans des catalyseurs a l'iridium depose sur des oxydes metalliques. *Journal of Electron Spectroscopy and Related Phenomena* **1975**, *6*, 17–26.

(81) Folkesson, B.; Bjorøy, M.; Pappas, J.; Skaarup, S.; Aaltonen, R.; Swahn, C.-G. ESCA Studies on the Charge Distribution in Some Dinitrogen Complexes of Rhenium, Iridium, Ruthenium, and Osmium. *Acta Chemica Scandinavica* **1973**, *27*, 287–302.

(82) Nyholm, R.; Berndtsson, A.; Martensson, N. Core level binding energies for the elements Hf to Bi (Z=72-83). *Journal of Physics C: Solid State Physics* **1980**, *13*, L1091–L1096.

(83) Terreros, P.; Pastor, E.; Fierro, J. Hept-1-ene hydroformylation on phosphinated polystyrene-anchored rhodium complexes. *Journal of Molecular Catalysis* **1989**, *53*, 359–369.

(84) Terreros, P.; Pastor, E.; Fierro, J. L. G.; Palacios, J. M. Radial distribution of heterogenized hydroformylation Rh complexes in phosphinated polystyrene beads. *Surface and Interface Analysis* **1990**, *15*, 279–285.

(85) Contour, J. X-ray photoelectron spectroscopy and electron microscopy of Pt\$z.sbnd;Rh gauzes used for catalytic oxidation of ammonia. *Journal of Catalysis* **1977**, *48*, 217–228.

(86) Carvalho, M.; Wieserman, L. F.; Hercules, D. M. Spectroscopic Characterization of Wilkinson's Catalyst Using X-ray Photoelectron Spectroscopy (ESCA). *Applied Spectroscopy* **1982**, *36*, 290–296.

(87) Fierro, J. L. G.; Palacios, J. M.; Tomas, F. An analytical SEM and XPS study of platinum-rhodium gauzes used in high pressure ammonia burners. *Surface and Interface Analysis* **1988**, *13*, 25–32.

(88) Hedman, J.; Klasson, M.; Nilsson, R.; Nordling, C.; Sorokina, M. F.; Kljushnikov, O. I.; Nemnonov, S. A.; Trapeznikov, V. A.; Zyryanov, V. G. The Electronic Structure of Some Palladium Alloys Studied by ESCA and X-ray Spectroscopy. *Physica Scripta* **1971**, *4*, 195–201.

(89) Nefedov, V. X-ray photoelectron spectra of halogens in coordination compounds. *Journal of Electron Spectroscopy and Related Phenomena* **1977**, *12*, 459–476.

(90) Segall, M. D.; Shah, R.; Pickard, C. J.; Payne, M. C. Population analysis of plane-wave electronic structure calculations of bulk materials. *Physical Review B* **1996**, *54*, 16317–16320.

(91) Salmeron, M. From Surfaces to Interfaces: Ambient Pressure XPS and Beyond. *Topics in Catalysis* **2018**, *61*, 2044–2051.

(92) Weatherup, R. S.; Wu, C. H.; Escudero, C.; Pérez-Dieste, V.; Salmeron, M. B. Environment-Dependent Radiation Damage in Atmospheric Pressure X-ray Spectroscopy. *The Journal of Physical Chemistry B* **2018**, *122*, 737–744.
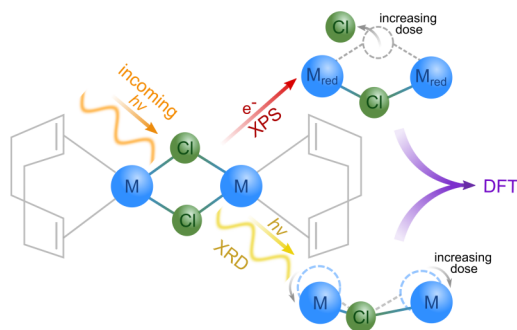
Figure 9: Table of Contents Figure